ORIGINAL PAPER

What can we learn from geothermobarometry at the dacitic Doña Juana Volcanic Complex (Colombia)? Implications for understanding Pleistocene crystal mushes and pre-eruptive storage conditions in the Northern Andes

César Bucheli[1] · Natalia Pardo[1] · Patricia Larrea[2] · Cristina de Ignacio[3] · Ana María Correa-Tamayo[4] · Marcelo Arnosio[5] · Bernardo A. Pulgarín[4]

Abstract

We present a reconstruction of the physicochemical conditions of melts in the Pleistocene storage and plumbing system of the Doña Juana Volcanic Complex (SW Colombia): a poorly known, potentially active polygenetic volcano of dacitic composition comprising four major edifices and showing periods of long quiescence. Compositional data for plagioclase, amphibole, pyroxene, and Fe-Ti oxides were combined with new and existing whole-rock data from representative eruptive products, allowing for the implementation of equilibrium tests and geothermobarometry calculations within an established stratigraphic, petrographic, and geochronological framework. Textural and geochemical variabilities of all mineral phases suggest the existence of a trans-crustal magmatic system feeding the Pleistocene eruptions of Doña Juana, and cyclic rejuvenation of a crystal mush following each volcano edifice collapse. The assemblage of different crystal cargos before magma recharge and final eruption is attested by (i) the coexistence of equilibrium and disequilibrium textures and variable compositions in crystals of all studied species, (ii) felsic cores in antecrysts, (iii) mafic overgrowth rims, and (iv) significantly less differentiated microcrysts relative to the composition of meso- and macrocrysts. By integrating multiple mineral-only and mineral-liquid geothermobarometers, after careful textural analyses, we estimate the intensive parameters of the mush–melt interaction zone of the plumbing system in the middle crust, providing a preliminary view of the architecture of a trans-crustal magmatic system in a complex tectonic setting at a previously understudied area of the north-Andean volcanic zone.

Keywords Crystal Mush · Dacite · Geothermobarometry · Northern Andes · Trans-Crustal Magmatic System

Communicated by Dante Canil.

✉ César Bucheli
ca.bucheli@uniandes.edu.co

Natalia Pardo
n.pardo@uniandes.edu.co

[1] Departamento de Geociencias, Universidad de Los Andes, Bogotá, D.C, Colombia

[2] Departamento de Geología, Facultad de Ciencias Físicas y Matemáticas, Universidad de Chile, Santiago, Chile

[3] Departamento de Mineralogía y Petrología, Facultad de Ciencias Geológicas, Universidad Complutense, Madrid, Spain

[4] Servicio Geológico Colombiano, Bogotá, D.C, Colombia

[5] IBIGEO–Universidad Nacional de Salta–CONICET, Salta, Argentina

Introduction

Active calc-alkaline volcanism at the Northern Andean Volcanic Zone (Thorpe and Francis 1979; Stern 2004) has been extensively explained as related to the oblique subduction of the oceanic Nazca plate beneath northwestern South America (Fig. 1a), at an average rate of 5–7 cm/yr (Pennington 1981; Droux and Delaloye 1996; Trenkamp et al. 2002; Monsalve-Bustamante 2020). Here, the Nazca subduction system is rather complex (Thorpe and Francis 1979; Stern 2004) with at least three slab portions plunging at different dipping angles and orientations (Pennington 1981; Gutscher et al. 1999; Marcaillou et al. 2008; Vargas and Mann 2013; Yarce et al. 2014; Idárraga-García et al. 2016; Sun et al. 2022; Mojica Boada et al. 2022). Their association to tears, colliding oceanic ridges and segmented rifts (Hall and Wood
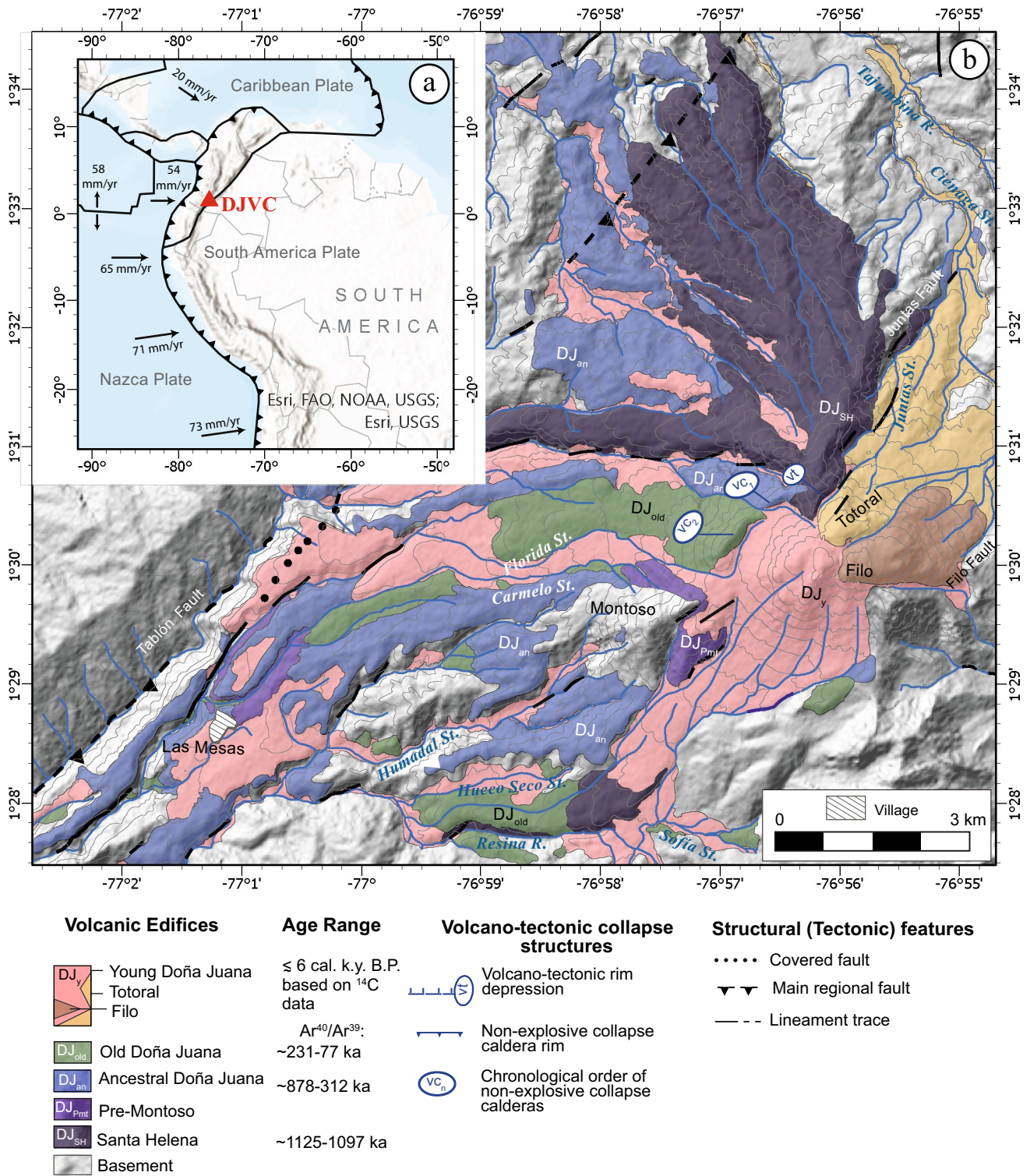
Fig. 1 Studied location; (**a**) Location of Doña Juana Volcanic Complex (DJVC; red triangle) at SW Colombia in the northwestern corner of South America; (**b**) Simplified 1:50,000 geological map of the DJVC, SW Colombia, modified from Pardo et al (2019, 2023). Pleistocene ages were obtained by ⁴⁰Ar/³⁹Ar. Holocene ages determined by.¹⁴C (Pardo et al. 2023)

1985; Barberi et al. 1988; Gutscher et al. 1999), results in the segmentation of the arc in Colombia (Monsalve-Bustamante 2020). In this context, eruptive products might reveal details of complex storage and plumbing systems feeding large, Pleistocene–Holocene polygenetic structures (Smith and Németh 2017), the evolution of a ~ 50–60-km-thick continental crust (Mojica Boada et al. 2022), and their subsequent implications for volcanic hazard management.

Geophysical and petrological data obtained over the last decade at arc volcanoes worldwide consistently reveal that large trans-crustal magmatic systems (TCMSs) dominated by crystal mushes supply polygenetic volcanism (Bachmann and Huber 2016; Cashman et al. 2017; Sparks et al. 2019; Giordano and Caricchi 2022; Petrone et al. 2022). Intrusion rates, geometry, volumes, and the temperature contrast with the surrounding environment dictate the yield strength required to initiate melt convection. Reactive flow and compaction-driven segregation from the mushes, remobilization, and melt segregation, together with density gradients relative to the crustal structure, control melt migration into shallower depths and the generation of eruptible magma (Humphreys et al. 2006; Solano et al. 2012; Ward et al. 2014; Comeau et al. 2015). Thus, vertically extensive TCMSs favor open-system differentiation processes such as crustal assimilation and fractional crystallization (DePaolo 1981; James and Murcia 1984; Hildreth and Moorbath 1988), magma mixing (Anderson 1976; Sparks et al. 1977; Gardner et al. 1995a, b; Smith et al. 2009), and mafic recharge from depth (Annen and Sparks 2002; Macías et al. 2017). While the chemical nature of the magma seems to be defined in the lower and middle crust, the final mineralogy and textural diversity increase in the shallow reservoirs upon variable ascent and crystallization paths (Annen et al. 2006; Sparks et al. 2019).

To contribute to the understanding of the poorly known storage and plumbing systems of large polygenetic volcanoes in Colombia (Northern Andes), we studied the Pleistocene products of the remote Doña Juana Volcanic Complex (DJVC; Fig. 1a, b). The DJVC is a long-dormant but potentially active center in SW Colombia, last erupted in the late nineteenth century (Pardo et al. 2023). Coeval mafic ignimbrites grouped as the Granatífera Tuff (hosting basalt to basaltic andesite volcanic bombs, as well as mantle and lower-crustal xenoliths exposed to the west of the study area; Weber et al. 2002), reveal a hot thermal regime within this arc segment related to the youngest lithospheric foundering known within the Andes (Bloch et al. 2017; Zieman et al. 2023, 2024).

Despite the variation between effusive and explosive eruptions known for the DJVC in the past million years, the mineral association, as well as major and trace element compositions of its products, has been monotonously dacitic (Pardo et al. 2019). Here, we investigate microscale textural and compositional variations within the predominant crystal phases of lavas and juvenile pyroclasts produced throughout the Pleistocene at the DJVC (Pardo et al. 2019). Thus, we apply multiple mineral-only as well as mineral-liquid geothermobarometers passing phase equilibrium tests, aiming to constrain the intensive parameters (pressure, P; temperature, T; composition, X; logarithm of oxygen fugacity, $\log f O_2$) characterizing crustal storage levels over multiple stages of the volcanic edifice's growth and collapse before the establishment of its most recent (Late Holocene) lava-dome complex.

Volcanological and stratigraphic background

The DJVC is located within the northernmost active volcanic segment of the Andes, specifically, as part of the volcanic arc in Colombia (Pennington 1981; Gutscher et al. 1999; Monsalve-Bustamante 2020; Fig. 1a). The DJVC consists of three large Pleistocene volcanic edifices and a Holocene lava-dome complex built over a polymetamorphic basement of Lower Cretaceous and pre-Mesozoic units intruded by Neogene igneous plutons, and locally overlain by a Miocene sedimentary formation (Pardo et al. 2019). Pleistocene DJVC products are coeval to mafic ignimbrites from a nearby but unknown source, known as the Granatífera Tuff (Weber et al. 2002). Components of this unit are known to be samples from the lower crust, sub-arc mantle, and juvenile arc magmas; and their composition is regarded as a close representative to that of primary melts in the region (Zieman et al. 2023, 2024).

The morpho-structural setting of the DJVC, as well as the stratigraphic and geochronological record, suggests at least five eruptive epochs associated with the construction and destruction of the three Pleistocene volcanic edifices (Pardo et al. 2019). The destruction stages are marked by overlapping volcano-tectonic collapse structures truncating each edifice (vt, vc_1, and vc_2, respectively; Fig. 1b). The eldest volcanic edifice—Santa Helena (DJ_{SH})— mostly consists of three lava flow formations with groundmass $^{40}Ar/^{39}Ar$ dates of ~ 1.1 ± 0.004 Ma. The DJ_{SH} is followed in age by the Ancestral Doña Juana edifice (DJ_{An}), whose two eldest units correspond to lava flow formations with biotite $^{40}Ar/^{39}Ar$ dates of 878 ± 2.8 ka. These lava flows are stratigraphically followed by a monolithologic debris avalanche deposit and correlated lahar deposits. Biotite retrieved from the predominant dacitic blocks of the debris avalanche deposits yielded an $^{40}Ar/^{39}Ar$ age of 778 ± 7 ka. The youngest DJ_{An} formation consists of block-and-ash flow deposits and correlated lahar deposits. Biotite and amphibole within the predominant juvenile blocks of the block-and-ash flows yielded $^{40}Ar/^{39}Ar$ ages between 696 ± 12 ka and 312 ka ± 28.8 ka. Lastly, the Old Doña Juana edifice (DJ_{Old}) groups a pyroclastic

formation—with $^{40}Ar/^{39}Ar$ dates of 231 ± 13.3 ka from plagioclase in a pumice block—and three lava flow formations, one of which yields an $^{40}Ar/^{39}Ar$ date of 80.4 ± 1.9 ka.

The Holocene edifice comprises the summit lava-dome complex and its correlative pyroclastic products (DJ_{Yn}; Fig. 1b) filling the youngest vc_2 summit depression, thus unconformably overlapping DJ_{Old} products. The last DJ_{Yn} eruption occurred in the late nineteenth century, with multiple lava-dome growth and explosive-disruption phases, and two major Vulcanian to sub-Plinian phases in 1899 CE that produced fallout and pyroclastic flows affecting the inhabited Las Mesas village (Pardo et al. 2023). Here, we leave the Holocene geochemistry for future work and focus our attention on describing the storage and plumbing system developed over the construction and destruction of DJ_{SH}, DJ_{An}, and DJ_{Old}, before the last major volcano-tectonic collapse.

Methods

A whole-rock ICP-MS dataset of 24 samples (Supplementary Material SMA1) was used in combination with polished thin sections prepared at the Servicio Geológico Colombiano (SGC; Pardo et al. 2016). Whole-rock analyses were executed at ActLabs S.A.S (Colombia) by IFusion CP(WRA) for major elements, and Fusion ICP/MS(WRA4B2) for trace elements. Major and trace elements were obtained following Package 4Lithores (which is a combination of 4B and 4B2-res methods). Samples were prepared and analyzed in a batch system. Each batch contained a method reagent blank, certified reference material, and 6% replicates. Samples were mixed with a flux of lithium metaborate and lithium tetraborate and fused in an induction furnace. The molten material was immediately poured into a solution of 5% nitric acid containing an internal standard and mixed continuously until completely dissolved. The samples were run for major oxides and selected trace elements (4B) on an ICP-MS. Calibration was performed using 14 prepared USGS and CANMET certified reference materials. One of the 14 standards was used during the analysis for every group of ten samples. Totals between 98.5% and 101% were considered as acceptable. If results came out lower, samples were scanned for base metals. Low reported totals may indicate sulfate being present or other elements (e.g., Li) which would not normally be scanned for. Samples with low totals, however, were automatically re-fused and reanalyzed.

Samples fused under code 4B2 were diluted and analyzed by ICP-MS. Three blanks and five controls (three before the natural samples, and two after) were analyzed per group of samples. Duplicates were fused and analyzed every 15 samples. Instrument was recalibrated every 40 samples. The loss on ignition (LOI)—which includes H_2O^+, CO_2, S, and other volatiles—was determined from the weight loss after igniting the sample at 1000 °C for 2 h. Concentrations of major elements in standard reference materials replicated certified values with a precision better than 5.08%. Quality Control details, and further information on precision and accuracy estimations are presented within the Supplementary Material SMA1.

Optical petrography was carried out for textural and mineralogical inspection, as well as for modal proportion counting based on a dense grid of 1000 points per section for a total of 14 samples of the DJVC (Supplementary Material SMA2). From said total, a subset of representative samples of the main lithostratigraphic units within the complex was chosen for carbon-coating and Electron Probe Micro Analysis (EPMA): three (3) samples correspond to DJ_{SH}, five (5) to DJ_{An}, and five (5) to DJ_{Old}. Crystals were subdivided by size according to the length of their longest visible axis (L) into microcrysts (L $\leq$ 100 µm), mesocrysts (100 µm < L < 300 µm) and macrocrysts ($\geq$ 300 µm).

Carbon-coated polished thin sections were measured with a JEOL superprobe JXA-8900 M at the Centro Nacional de Microscopía Electrónica of the Universidad Complutense de Madrid (UCM, Spain) for mineral chemistry (spot analyses). Analysis was carried out with a voltage of 15 kV, 20 nA current intensity, and an incident beam diameter of 5 µm (10 s at peak and 5 s at valleys) as running conditions. A defocused beam (10 µm) was used for amphibole to avoid Na loss, and the ZAF correction system was applied (corrections for matrix effects as a function of atomic number, Z; absorption of the radiation generated, A; and secondary fluorescence, F). At least two spots were analyzed in each crystal, distinguishing core, mantle, and rim data when possible. Spots within patchy zoned crystals whose location and characteristics did not match with a 'core' or 'mantle' label were marked as 'patch' (Supplementary Material SMA3). Analytical precisions between 0.5% and 6% were reached for oxides with concentrations higher than 1.5 wt%, and less than 10% for oxides with lower concentrations. Standard reference materials from the Smithsonian Institution (Jarosewich et al. 1980) were used for EPMA calibration (see further details in Supplementary Material SMA3). These standards were checked for internal consistency by comparing theoretical k values (from known compositions and ZAF corrections) to measured k values, so that the ratio between both was close or equal to 1. The length of the 2D major axis of each probed mineral was also measured on scaled BSE images using ImageJ (Schneider et al. 2012) for size-based classification. Glass compositions could not be accurately obtained due to the high microcrystalline nature of the samples' groundmass.

After excluding analyses with low totals and verifying resulting mineral structural formulas, a total of 942 analyses allowed for the compositional classification of the main mineral phases (plagioclase, amphibole, biotite, orthopyroxene,

clinopyroxene, and Fe-Ti oxides) of representative lavas and juvenile pyroclasts.

To obtain realistic results from the application of geothermobarometers, we avoided measuring pseudomorphs and mafic minerals with textures exhibiting oxidation or other reaction rims, clearly indicating disequilibrium conditions with the pre-eruptive melt. In the case of plagioclase, we probed all crystal textures since most of the Pl crystals show subhedral overgrowth rims which could potentially provide pre-eruptive equilibrium conditions. Also, oscillatory zoning is common in all Pl textures, and it is worth examining the compositional variation between core, mantle, and rims potentially growing in equilibrium with the surrounding melt. For geothermobarometry models based on mineral-liquid pairs, only the data that passed equilibrium tests (i.e., were in the equilibrium zone of Rhodes or Rhodes-type diagrams; Rhodes et al. 1979) were considered for analysis and discussion. The nominal melt composition used for these equilibrium tests corresponds to that of the bulk rock (decision that will be further explained in the discussion section). Additional information on the composition of pre-eruptive melts was obtained from the compositions of clinopyroxene and amphibole through the chemometric machine learning models of Higgins et al., (2022). Since these chemometric models provide the composition of melts in equilibrium with different sections within crystals, they were used to track the compositional evolution of DJVC melts across different stages of fractional crystallization, but not for mineral-liquid equilibrium tests.

Results

Whole-rock geochemistry and petrography

Studied samples are subalkaline, calc-alkaline dacites, and rarely andesites (Fig. 2a), with a narrow range of silica contents (59.05 wt% $< SiO_2 < 66.82$ wt%), $Na_2O + K_2O$ values between 4.12 wt% and 6.46 wt%, and Mg# between 55.82 and 41.96 on anhydrous basis (Supplementary Material SMA1). Representative samples within each volcanic edifice show oscillations in the concentrations of SiO_2, K_2O, FeO_T, and CaO concentrations (Fig. 2b).

Major elements bivariate plots (Fig. 3) show decreasing trends of CaO, TiO_2, MgO, FeO_T, and MnO concentrations with increasing SiO_2 content, suggesting a compatible behavior. In contrast, K_2O contents show an increasing trend, reflecting its incompatible behavior, and Na_2O, Al_2O_3, and P_2O_5 concentrations show scattered patterns.

Trace elements (Supplementary Material SMA1) show patterns of LREE vs. HREE enrichment when compared to the chondrite (Fig. 4a; McDonough and Sun 1995), and enriched LILEs vs. HFSE patterns, with a marked Pb positive anomaly and a Nb negative anomaly when compared to the N-MORB (Fig. 4b; Sun and McDonough 1989). Typical LILEs and HFSE such as Rb (Fig. 4c), Cs, Ba, U, Th, and Pb increase with silica content, whereas Zr (Fig. 4d), Hf, and Nb mostly show a dispersed pattern. Typical compatible elements, such as V (Fig. 4e) and Sc, together with HREE (e.g., Lu, Fig. 4f) and Y (Fig. 4g) show clear negative trends, whereas Sr, Eu (Fig. 4h), LREE, and MREE show dispersed but slightly negative trends.

The negative trends of bivariate plots are consistent with the crystallization of the mineral phases identified in petrography. Studied thin sections (Supplementary Material SMA2) are porphyritic, seriated, and show different proportions of euhedral to anhedral plagioclase (Pl) + amphibole (Amp) + clinopyroxene (CPx) ± orthopyroxene (OPx) ± biotite (Bt) ± quartz (Qz) + iron and titanium oxides (Fe-Ti oxides) ± apatite (Ap) ± zircon (Zr), and rare olivine (Ol) in a groundmass with variable contents of glass, microcrysts, and vesicles, occasionally showing flow texture. In some samples, the hydrated mafic minerals (i.e., Amp and Bt) are completely replaced by Fe-Ti oxides (pseudomorphism: pmf). Additionally, most samples exhibit the presence of cognate enclaves of CPx + OPx + Pl + Fe-Ti oxides, and Pl + Amp + Fe-Ti oxides with variable OPx content, showing a distinctive microphaneritic texture.

The crystal contents within the subset of samples selected for EPMA analysis (Supplementary Material SMA3; Fig. 2) range from 13% to 29% in DJ_{SH}, 29% to 45% in DJ_{An}, and 12% to 37% in DJ_{Old}. In all samples, coexisting equilibrium and disequilibrium textures were identified in all mineral phases regardless of size (Supplementary Material SMA2, Supplementary Material B). The studied DJ_{An} samples (lavas and pyroclasts) exhibit green and brown Amp, and higher Bt and Ap contents compared to DJ_{SH} samples (all lavas). Additionally, the diversity of textural variation within each mineral phase is higher in DJ_{An} when compared to DJ_{SH} samples, including marked Amp and CPx zoning, CPx with Amp rims, Bt with Amp rims, and Qz with pyroxene rims. However, equilibrium textures are predominant in all phases (Supplementary Material SMA2). In comparison, DJ_{Old} samples (one pyroclast, and mostly lavas) show relatively higher contents of Qz macrocrysts with graphic textures, a higher occurrence of disequilibrium textures in all phases, and the occasional presence of Ol.

Mineral chemistry

Details of mineral compositions obtained in each analyzed spot within each textural type and crystal size are compiled within Supplementary Material SMA3. We summarize the main characteristics below.
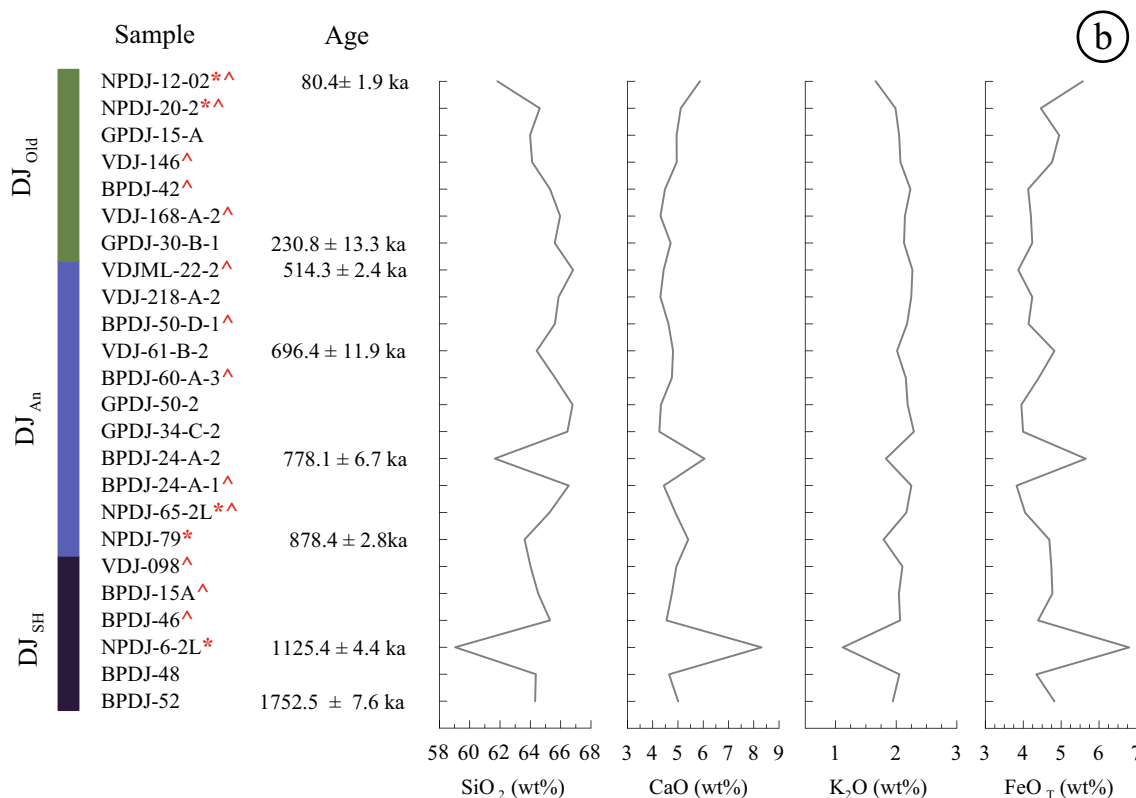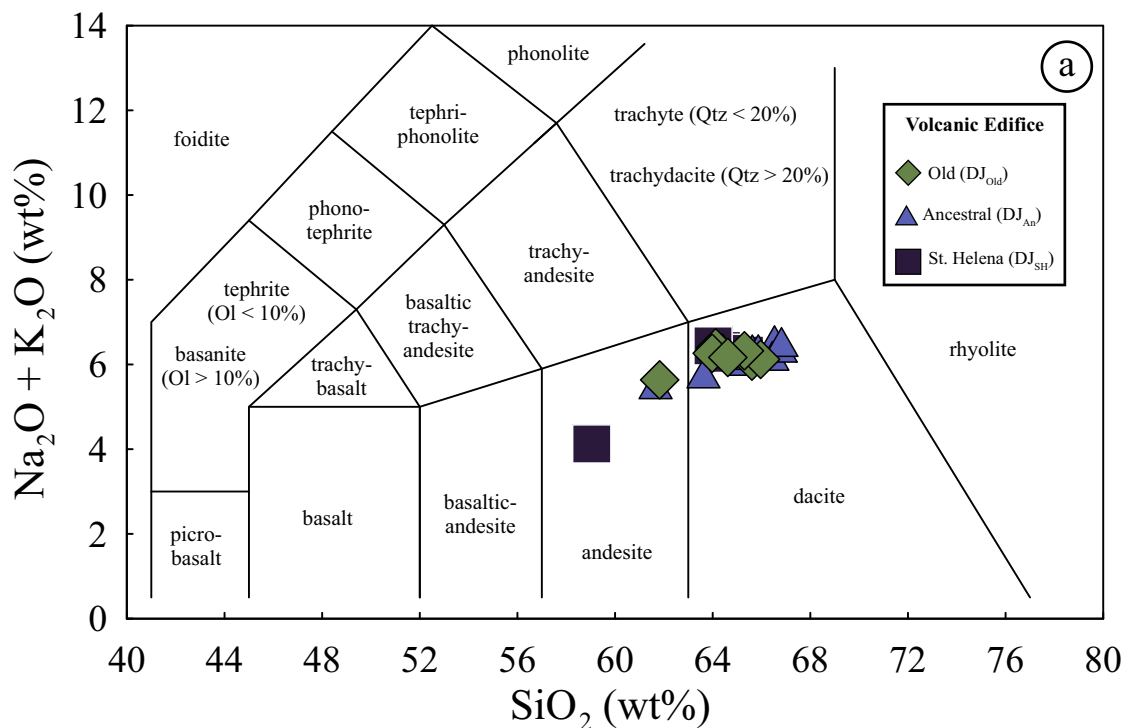
Fig. 2 Whole-rock geochemical variation (anhydrous basis) within Pleistocene DJVC units. **a** Total Alkali–Silica plot (Le Bas et al. 1986; Le Maitre et al. 2002) showing the restricted variation over time; (**b**) same data plotted with stratigraphic position to best show variations of main major elements. Data retrieved from Pardo et al. (2019) except for those marked with "*," which were analyzed for this study. Samples marked with (^) were selected for EPMA analysis

Fig. 3 Bivariate plots for anhydrous, whole-rock major elements. (Data shown in Supplementary Material SMA1)

Volcanic Edifice

St. Helena (DJ$_{SH}$)   Ancestral (DJ$_{An}$)   Old (DJ$_{Old}$)
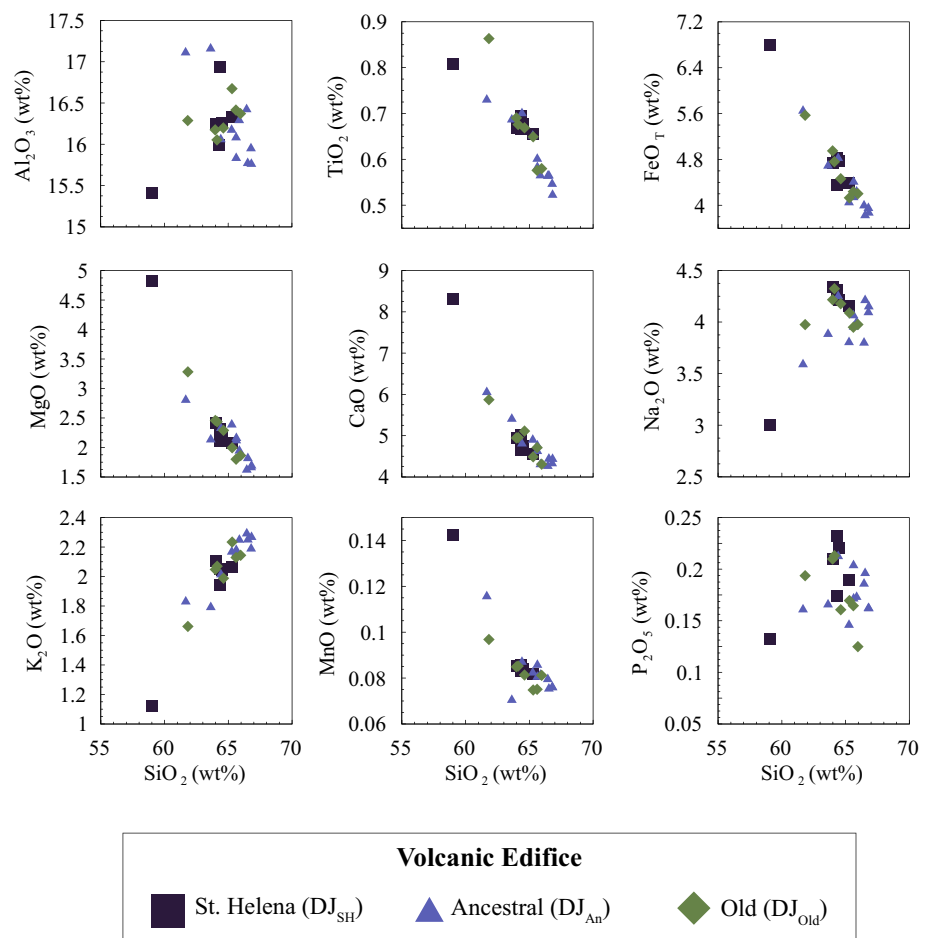
Plagioclase

Pl ($n = 437$) occurs predominantly as macrocrysts, mesocryst aggregates, or as free mesocrysts and microcrysts (Fig. 5). We identified four textural types (Fig. 5a–d′): (i) PlT1 comprises well-preserved crystals with oscillatory zoning and a thin overgrowth rim, ranging from euhedral to subhedral (PlT1a) and rounded anhedral (PlT1b). (ii) PlT2 includes euhedral to subhedral crystals showing a coarse sieved texture that encompasses most of the crystal or is concentrated in a peripheral zone, before an overgrowth rim thicker than in PlT1; (iii) PlT3 is distinguished by clean but anhedral cores with oscillatory or patchy zoning, surrounded by a peripheral mantle with a fine sieved texture and a subhedral to anhedral overgrowth rim; (iv) PlT4 groups plagioclases with corroded anhedral cores and a fine sieved texture that covers most of the crystal, surrounded by an anhedral to subhedral overgrowth rim of variable thickness. Some PlT4 cores are microaggregates and show patchy zoning. Many cores of macro- and mesocrysts show deformation twins and serrated grain boundaries.

All Pl textures range widely in composition regardless of crystal size and the position of the spot analyzed within each crystal (Fig. 5e; Supplementary Material SMA3.1). Plagioclase ranges in composition from An$_{19}$Ab$_{77}$Or$_4$ to An$_{80}$Ab$_{19}$Or$_1$, with PlT1 exhibiting the lowest An contents and PlT4 the highest. Most of the data fit into the andesine and labradorite fields, with a few data yielding bytownite and oligoclase. There are no systematic changes in plagioclase classification throughout stratigraphic position, although there are more oligoclase core specimens in DJ$_{Old}$ relative to DJ$_{An}$ and DJ$_{SH}$. Likewise, there are no variations in systematic classification according to size, textural type, or position within macro- and mesocrysts.

Compositions of plagioclase macro- and mesocrysts group into three main sets: (i) An$_{20-40}$, (ii) An$_{41-60}$, and (iii) An$_{61-80}$. Among macro- and mesocrysts, most crystals classified as (i) An$_{20-40}$ correspond to PlT1 anhedral cores and mantles (Fig. 5b′). In all samples, these felsic cores (An$_{20-40}$) commonly show deformation twins and lamellae, and coexist with quartz macrocrysts and Fe-Ti oxides microaggregates with exsolution lamellae. Some cores and mantles of all textures fall within (ii) An$_{41-60}$. Finally, most (iii) An$_{61-80}$ primarily correspond to PlT4 cores and mantles, including a few PlT2 and PlT3 mantles (Fig. 5d–d′).

Fig. 4 Whole-rock trace elements diagrams; (**a**) REE normalized to the Chondrite (McDonough and Sun 1995); (**b**) Spider diagram of concentrations normalized to the composition of the N-MORB (Sun and McDonough 1989); (**c–h**) Bivariate diagrams for select whole-rock trace elements. The complete dataset is shown in Supplementary Material SMA1
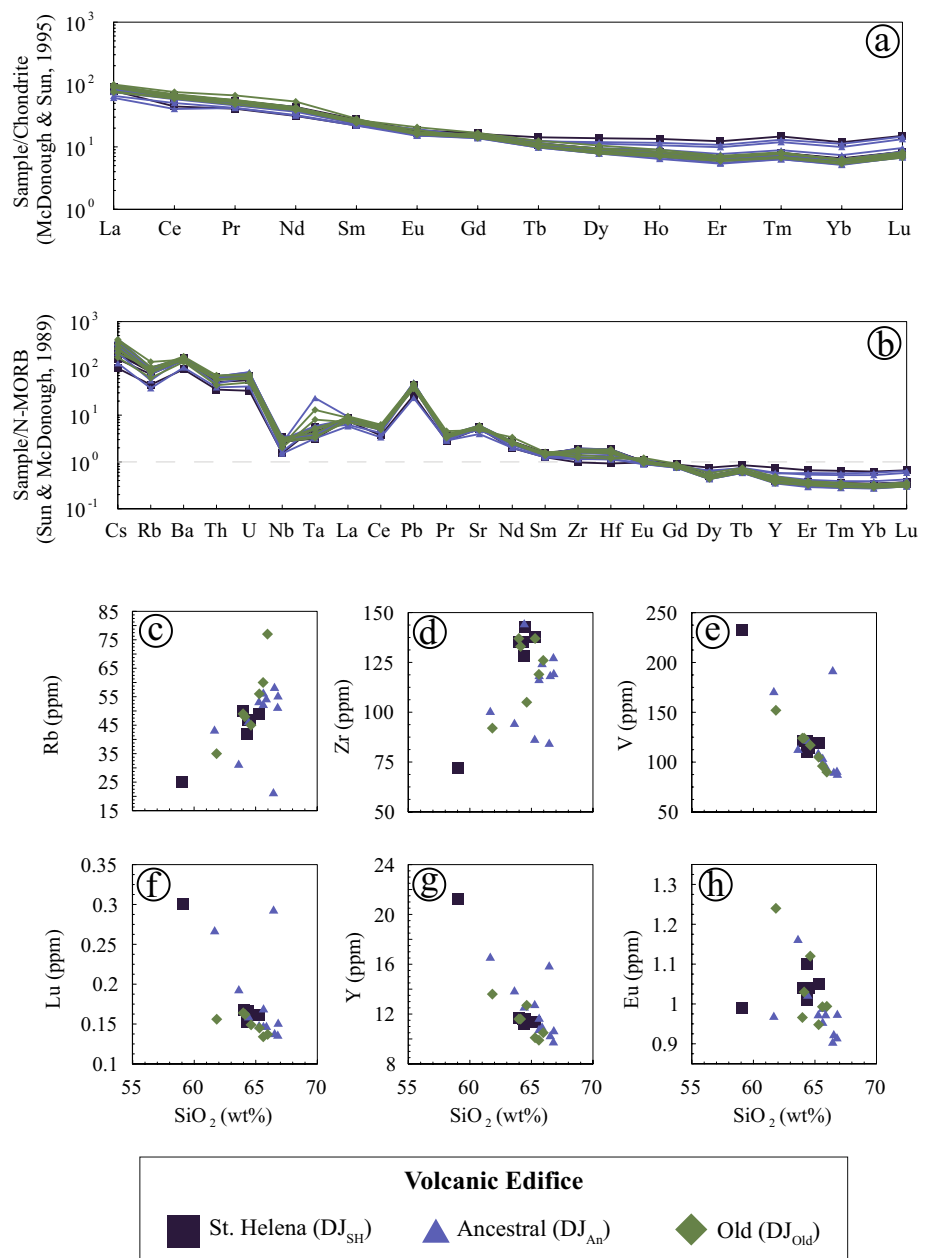
The Pl cores of the oldest units within each edifice are slightly displaced toward the felsic endmembers. Crystals from DJ_{SH} and DJ_{Old} show a slight increase in An contents within cores and rims of the youngest samples relative to the eldest. In addition, most PlT1 and PlT2 rims fall within sets (i) An_{20-40} and (ii) An_{41-60}, whereas most PlT3 and PlT4 rims fall within sets (ii) An_{41-60} and (iii) An_{61-80}. Also, groundmass microcrysts range in composition from $An_{31}Ab_{66}Or_3$ to $An_{65}Ab_{34}Or_2$ throughout all analyzed samples. Most microcrysts fall within set (ii) An_{41-60} in DJ_{SH} samples, within set (i) An_{20-40} in DJ_{An}, and within sets (ii) An_{41-60} and (iii) An_{61-80} in DJ_{Old}. Finally, for any compositional/textural group in any of the samples, there are several

examples of crystals where the An component is richer in their rims than in their corresponding cores (Supplementary Material SMA3.1).

Amphibole

Amp ($n = 184$) occurs as microaggregates or free mesocrysts and mostly microcrysts. We recognized three main textural types, many with concentric or patchy zoning (Supplementary material B): (i) AmpT1 includes clean, subhedral to euhedral crystals without reaction rims or showing a very thin Fe-Ti oxides rim; (ii) AmpT2 groups subhedral crystals with skeletal textures, some with concentric zoning and
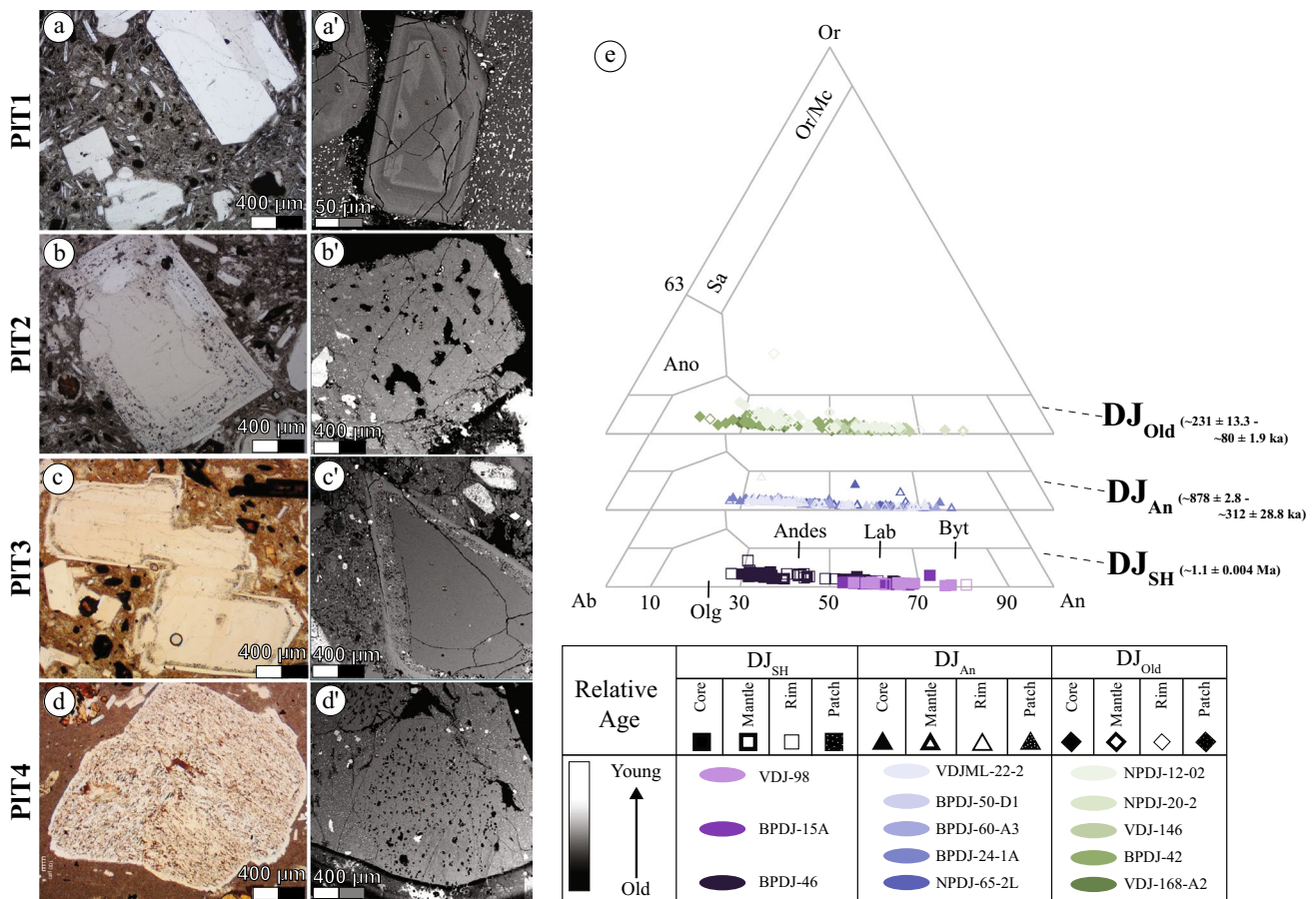
Fig. 5 Plagioclase textural and geochemical classification. Texture classes correspond to (a–a′) euhedral and clean PlT1, (b–b′) euhedral coarse sieved PlT2, (c–c′) subhedral to anhedral with an external thinly sieved mantle surrounded by an overgrowth rim; and (d–d′) anhedral dusty crystals, mostly corroded and showing an overgrowth rim. All textures range in composition from Bytownite to Oligoclase (e), irrespective of crystal size, spot location, or stratigraphic position

~10–20-μm-thick Fe-Ti oxides rim; and (iii) AmpT3 comprises subhedral to anhedral and corroded crystals, mostly replaced by Fe-Ti oxides (pseudomorphs).

The validity of Amphibole analyses and their classification was tested using AMFORM (Ridolfi et al. 2018), and follows the nomenclature resulted in Amp-TB2 (Ridolfi 2021). Amp range widely in composition irrespective of crystal size and the position of the spot analyzed within each crystal. Most of the data fit into the tschermakite-pargasite, Mg-hastingsite and Mg-Hornblende classes (Supplementary Material SMA3.2). Although there are no systematic classification changes throughout stratigraphic position, amphibole in DJ_{SH} shows only a tschermakite-pargasite/Mg-hastingsite composition, whereas Mg-hornblende (i.e., a phase slightly richer in silica and poorer in $Na + K$) is dominant throughout DJ_{An} and up to the youngest samples of DJ_{Old}, where the content of pargasitic amphibole increases again. This is readily observed in Fig. 6a, where bivariate plots of SiO_2, Al_2O_3, and Na_2O vs. Mg# show two distinct compositional groups.

Overall, Mg# of macro- and mesocrysts ranges from 57 to 76, generally overlapping with Mg# 63–75 obtained in microcrysts (free and interstitial). Zoned mesocrysts (common in DJ_{An} and DJ_{Old}) show cores with Mg# 57–75 and corresponding rims of Mg# 72 and 59, respectively. Normal and reverse zoning is detected by Mg#. There are no systematic changes in Mg# with stratigraphic position, although cores and rims of macro- and mesocrysts are generally lower in Mg# within the oldest samples of DJ_{SH} and DJ_{Old} than in their younger counterparts for each respective edifice. Average Amp Mg# is 70 ± 3 in DJ_{SH} ($n = 41$), 67 ± 5 in DJ_{An} ($n = 96$), and 68 ± 4 in DJ_{Old} ($n = 47$; Supplementary Material SMA3.2).

Pyroxene

Pyroxene (Px; $n = 192$) is present mostly as CPx meso- and microcrysts (Fig. 6b), along with variable contents of OPx (Fig. 6c). We distinguished (i) subhedral to euhedral clean crystals (PxT1), some included within Amp, and (ii)
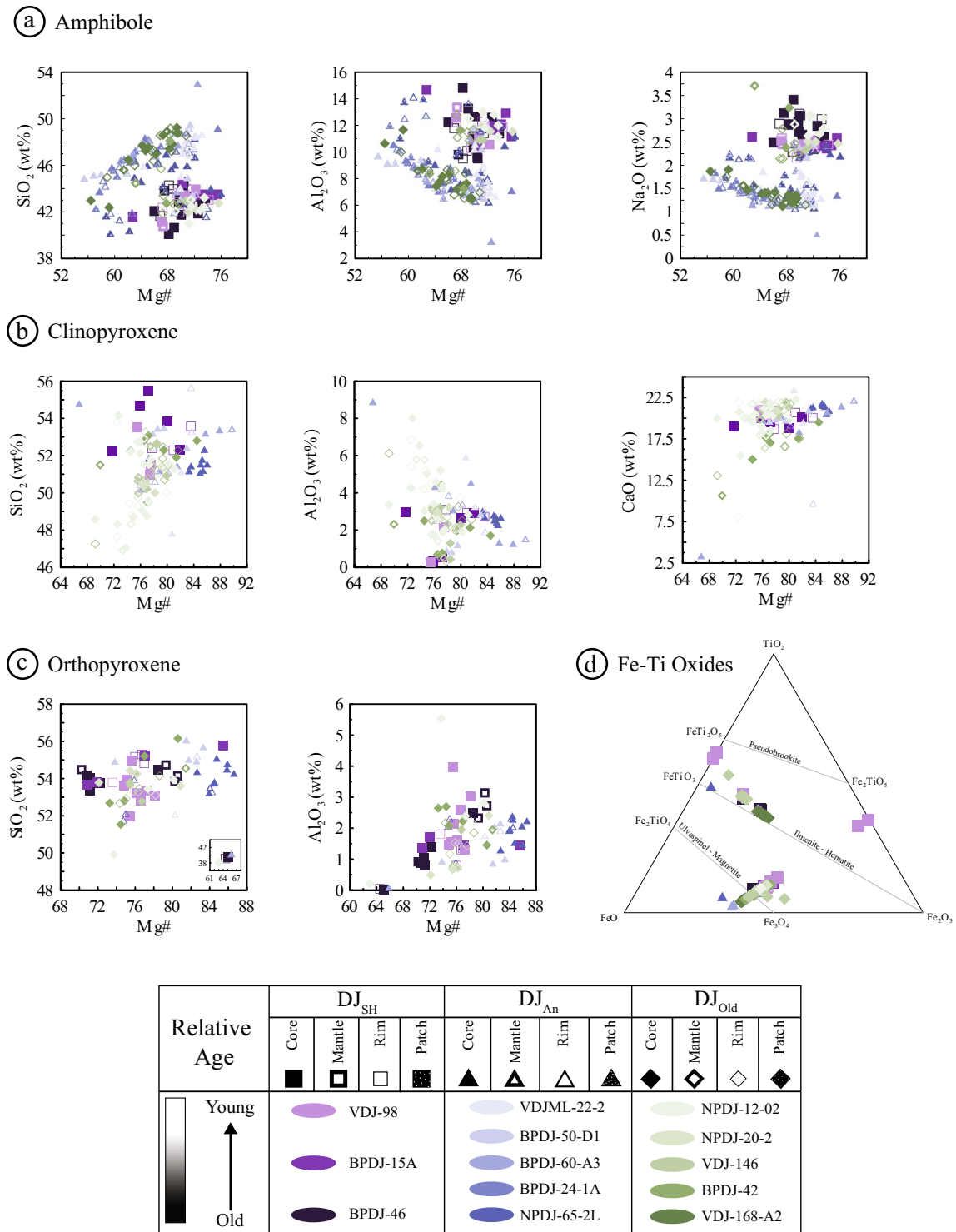
Fig. 6 Dominant mafic mineral compositions in the studied units, showing representative bivariate plots for (**a**) amphiboles, (**b**) clinopyroxenes, (**c**) orthopyroxenes, and (**d**) Fe-Ti oxides. Individual textures are illustrated in SD3

subhedral to anhedral crystals with skeletal texture and resorbed edges, some with coronae of $Amp \pm Pl + Fe$-Ti oxides (PxT2). In addition, there are (iii) Px microaggregates bordered by an overgrowth rim (Supplementary Material B).

CPx (Supplementary Material SMA3.3) classifies as augite and ranges between $En_{42}Wo_{44}Fs_{14}$—$En_{48}Wo_{42}Fs_{10}$ in DJ_{SH}, $En_{42}Wo_{42}Fs_{14}$—$En_{66}Wo_{21}Fs_{13}$ in DJ_{An}, and $En_{39}Wo_{47}Fs_{15}$—$En_{57}Wo_{21}Fs_{22}$ in DJ_{Old}. OPx

(Supplementary Material SMA3.4) classifies as enstatite and ranges $En_{64}Wo_0Fs_{36}$—$En_{83}Wo_2Fs_{14}$ in DJ_{SH}, $En_{71}Wo_3Fs_{25}$—$En_{83}Wo_3Fs_{15}$ in DJ_{An}, and $En_{66}Wo_{12}Fs_{22}$—$En_{79}Wo_2Fs_{18}$ in DJ_{Old}. Average pyroxene Mg# is 76 ± 4 in DJ_{SH} ($n = 41$), 82 ± 5 in DJ_{An} ($n = 49$), and 76 ± 4 in DJ_{Old} ($n = 102$). Normal and reverse zoning is recorded by Mg#.

There are no clear linear trends in bivariate plots of CPx, with SiO_2, Al_2O_3, and CaO contents best showing variations with Mg# (Fig. 6b). In OPx, SiO_2 and Al_2O_3 show the most compositional variation with Mg#, although with significant scattering (Fig. 6c).

Fe-Ti oxides

Fe-Ti oxides ($n = 129$) are Ti-magnetite, magnetite (Mt), and ilmenite (Il) (Fig. 6d) appearing as microaggregates or free meso- and microcrysts scattered in the groundmass of all samples, sometimes forming reaction rims, or totally replacing mafic minerals. The largest mesocrysts show Mt-Il exsolution lamellae. Magnetite Mg# ranges between 2.8 and 11.7 ± 3 ($n = 16$; Supplementary Material SMA3.5) and ilmenite Mg# between 6.9 and 22.11 ± 7 ($n = 7$) in DJ_{SH}; 1.5and 3.7 ± 1 ($n = 23$) and 0.4 and 5.3 ± 2 ($n = 8$) in DJ_{An}, respectively; and 1.2 and 41.7 ± 8 ($n = 50$) and 3.8 and 22.7 ± 4 ($n = 25$) in DJ_{Old} (Supplementary Material SMA3.6).

In DJ_{SH} samples, magnetite shows several variation trends with upward stratigraphic position, including increases in TiO_2 (8.0–8.5 to 9–13 wt%), Al_2O_3 (1.0–1.5 to 3.0–5.0 wt%), and MgO contents (1.0–1.5 to 2.0–4.0 wt%), along with a decrease in MnO (0.7–0.5 to 0.0–0.2 wt%), while Cr_2O_3 is low and relatively constant (0.1–0.3 wt%) (Supplementary Material SMA3.5). Ilmenite exsolution lamellae also mimic these trends, with geikielite (MgO) components increasing from 10% to 15% but showing constantly low values ($< 1\%$) in their pyrophanite component (MnO) (Supplementary Material SMA3.6).

There is a sharp change in magnetite geochemistry at the onset of DJ_{An}, with a decrease in TiO_2 (4.4–6.6 wt%), Al_2O_3 (1.6–2.6 wt%) and MgO (1.0–1.7 wt%), and a slight increase in MnO contents (0.4–0.5 wt%) compared to crystals from DJ_{SH}. Ilmenite exsolutions, in turn, are strongly enriched in their pyrophanite component (MnO = 6–8%) and almost lack a geikielite component (MgO < 2%). These trends are followed by an increase in magnetite TiO_2 contents at DJ_{Old}, starting from similar, 4.0–5.0 wt% at the onset of this edifice, and rising progressively to 5.0–8.0% and 6.0–10.0% toward the youngest sample (NPDJ-12-02), whereas the rest of elements do not show a significant variation. This youngest DJ_{Old} sample also contains opaque mineral inclusions in olivine crystals, which range from chromium–aluminum-rich magnetites (up to 20 wt% Cr_2O_3 and 12 wt% Al_2O_3) to chromium-bearing magnetites (2 wt% Cr_2O_3).

Ilmenites from NPDJ-12-02 are also different from other DJ_{Old} samples, containing higher geikielite components (MgO = 11–20%) and slightly lower pyrophanite components (MnO = 0.8–1.5%).

Other mineral phases

Biotite (Bt) mostly occurs as free macro- and mesocrysts, ranging in texture from (i) euhedral to subhedral clean crystals, some with a localized skeletal texture (BtT1); to (ii) subhedral crystals showing thin coronae of Pl + Fe-Ti oxides (BtT2); and (iii) anhedral crystals with skeletal textures and corroded edges bordered by a thick corona of oxidized Amp microcrysts or Amp + Pl + Fe-Ti oxides, or Amp + Px + Pl + Fe-Ti oxides (BtT3; Supplementary Material B). Despite this textural variation, biotite composition is relatively constant, with Mg# mainly ranging between 61 and 66 in DJ_{An} and DJ_{Old} but decreasing to between 59 and 56 in BtT3 oxidized crystals. All biotites contain between 3.9 and 4.5 wt% TiO_2, 0.2 and 0.8 wt% BaO, and 0.1 and 0.5 wt% F, the latter rising occasionally to 1 wt% in the rims of BtT2 and BtT3 crystals from DJ_{Old} (Supplementary Material SMA3.7).

Quartz (Qz) occurs in some samples as free macrocrysts and mesocrysts, ranging in textures (Supplementary Material B) from (i) anhedral crystals without disequilibrium textures, except for some dissolution embayments (QzT1), to (ii) anhedral crystals surrounded by a pyroxene corona (QzT2), or (iii) pseudomorphs completely replaced by pyroxene (QzT3). Remarkably, Qz with disequilibrium textures coexists with olivine mesocrysts and macrocrysts in sample NPDJ-12–02, which belongs to the uppermost lava flows sourced from DJ_{Old}.

Discussion

Equilibrium conditions and Geothermobarometry

One of the key quests in Andean dacites with complex mineral textures—such as the DJVC products—is to identify mineral phases in equilibrium with the melt to best approach the intensive parameters of pre-eruptive storage conditions. To do so, in this contribution, we first excluded data from interstitial crystals and microaggregates. In the case of plagioclase, we also excluded data with An_{20-40}, mostly corresponding to anhedral cores of macro- and mesocrysts, likely corresponding to evolved antecrysts. Since measuring melt inclusions was beyond the feasibility of this study, the implementation of mineral-liquid pair thermobarometers had to occur after considering several restrictions: first, the composition of the residual glass in our samples cannot be taken as representative of

the melt due to its abundant silica contents in all samples, and because fractional crystallization seems to be a prominent differentiation process in DJVC magmas. These factors—along with the high microcrystalline nature of the samples' groundmass—made EPMA measurements of glass unreliable. Another available source of melt compositional information were the chemometric reconstructions of melt compositions in equilibrium with Amp and CPx from the models of Higgins et al. (2022); however, these do not necessarily represent the immediately pre-eruptive melt since they may correspond to different sections within crystals (i.e., cores, mantles, etc.). Hence, we explored the potential state of chemical equilibrium by constructing and analyzing Rhodes and Rhodes-type diagrams (Rhodes et al. 1979) using bulk rock compositions as nominal representatives of the melt.

The limited geochemical variability of our dacitic samples throughout the geological record of the DJVC implied that, unsurprisingly, using the bulk rock composition of a sample for the mineral-liquid equilibrium tests of another did not yield significant differences in our results. Hence, we paired each macrocryst composition with its corresponding host whole rock and, in accordance, only such pairs showing compositional equilibrium were further used for mineral-melt thermobarometry estimations (Supplementary Material SMA3). In order to establish the compositional boundaries for equilibrium in the Rhodes diagrams, we used Putirka's (2008) partition coefficients: (i) Kd_{An-Ab} of 0.1 ± 0.05 for low-temperature (T < 1050 °C) and 0.27 ± 0.11 for high-temperature (T > 1050 °C) plagioclase, (ii) Kd_{Fe-Mg} of 0.29 ± 0.06 for orthopyroxene, and (iii) Kd_{Fe-Mg} of 0.28 ± 0.08 for clinopyroxene. In addition, we used the Kd_{Fe-Mg} of 0.39 ± 0.07 reported by Putirka (2016) for amphiboles.

After following these procedures, Pl data fit within the envelopes of the high (Fig. 7a) and low (Fig. 7b) temperature partition coefficients (Kds) for mineral-melt anorthite–albite components. A few cores remained outside the lowest limit of the high-temperature Kd (i.e., are more felsic than expected for a given nominal melt), and a few PlT4 data remained above the envelope of the low-temperature Kd (i.e., are more mafic than expected for a given nominal melt).

Data distribution in Rhodes' diagrams for ferromagnesian minerals is rather complex, with most of the Amp plotting outside equilibrium (Fig. 7c). Clino- and orthopyroxene data plotting above and below the equilibrium envelopes are mostly core data (Fig. 7d, e). We validated the CPx equilibrium conditions by evaluating the predicted vs. observed diopside–hedenbergite (DiHd) mineral components, with most data plotting close to the one-to-one line (within ± 10%; Fig. 7g; Putirka 2008). Therefore, when applying mineral-liquid thermobarometers we excluded all data plotting outside the equilibrium boundaries.

To verify the robustness of results from mineral-liquid pair thermobarometers, we also implemented multiple Amp-only models (Johnson and Rutherford 1989; Thomas and Ernst 1990; Schmidt 1992; Ridolfi et al. 2010; Ridolfi and Renzulli 2012; Mutch et al. 2016; Ridolfi 2021; Higgins et al. 2022; Médard and Le Pennec 2022) and CPx-only models (Petrelli et al. 2020; Wang et al. 2021; Higgins et al. 2022) to estimate storage pressures and temperatures (Fig. 8a, b; Supplementary Material SMA3). Thermobarometry results from models based on mineral-liquid equilibrium pairs presented in Fig. 8 (i.e., Putirka et al. 2003; Putirka 2008, 2016) only include data plotting within compositional equilibrium boundaries in Rhodes diagrams. The medians of crystallization pressures retrieved from Amp-only barometers published after (and including) Ridolfi and Renzulli (2012) and CPx-only barometers (Fig. 8a) range between 487 and 200 MPa in DJ_{SH}, 336 and 79 MPa in DJ_{An}, and 284 and 95 MPa in DJ_{Old}. All mineral-liquid barometers fall within these ranges except for Pl-liquid and OPx-liquid results, which is consistent with their corresponding estimation errors (± 400 and ± 210 MPa, respectively). Results from these last two models were excluded from further consideration. The lowest values correspond to those of the Amp-only barometer of Ridolfi and Renzulli (2012; 79 MPa) in DJ_{An}, and the Wang et al. (2021) CPx-only barometer (95 MPa) in DJ_{Old}. The lowest median value from the amphibole barometer was obtained from the core and mantle of a macrocryst, while the one from CPx barometry was obtained from a microcryst, facts that could be explained by the introduction of macrocryst-bearing melts into shallow reservoirs undergoing microcryst crystallization within the shallow plumbing system (Supplementary Material SMA3.8).

Similarly, we compare Amp-only and CPx-only with Pl-liquid (Putirka 2008), CPx-liquid (Putirka et al. 2003), and OPx-liquid (Putirka 2008) thermometers (Fig. 8b; Supplementary Material SMA3). Median crystallization temperatures are 1185–1009 °C for CPx, 1102 °C for Pl, 1077 °C for OPx, and 950–940 °C for Amp in DJ_{SH}; 1172–1032 °C for CPx, 1080 °C for Pl, and 850–828 °C for Amp in DJ_{An}, where no pyroxenes passed the equilibrium tests in the Rhodes' diagrams; and 1132–1106 °C for CPx, 1106 °C for Pl, 1059 °C for OPx, and 875–840 °C for Amp in DJ_{Old} (Supplementary Material SMA3.8).

In addition—and following Ghiorso and Evans (2008)—the compositions of coexisting titanomagnetites and ilmenites were used for estimating temperature and log$f$O$_2$ (Powell and Powell 1977; Spencer and Lindsley 1981; Andersen and Lindsley 1985) after confirming their equilibrium conditions (Bacon and Hirschmann 1988; Fig. 7f). Fe-Ti oxides pairs (Mt-Il) plotting outside equilibrium boundaries mainly correspond to exsolution lamellae and a few inclusions of Mt with Il exsolutions in amphibole. These yielded high TiO_2 contents (33 wt%), which we attribute
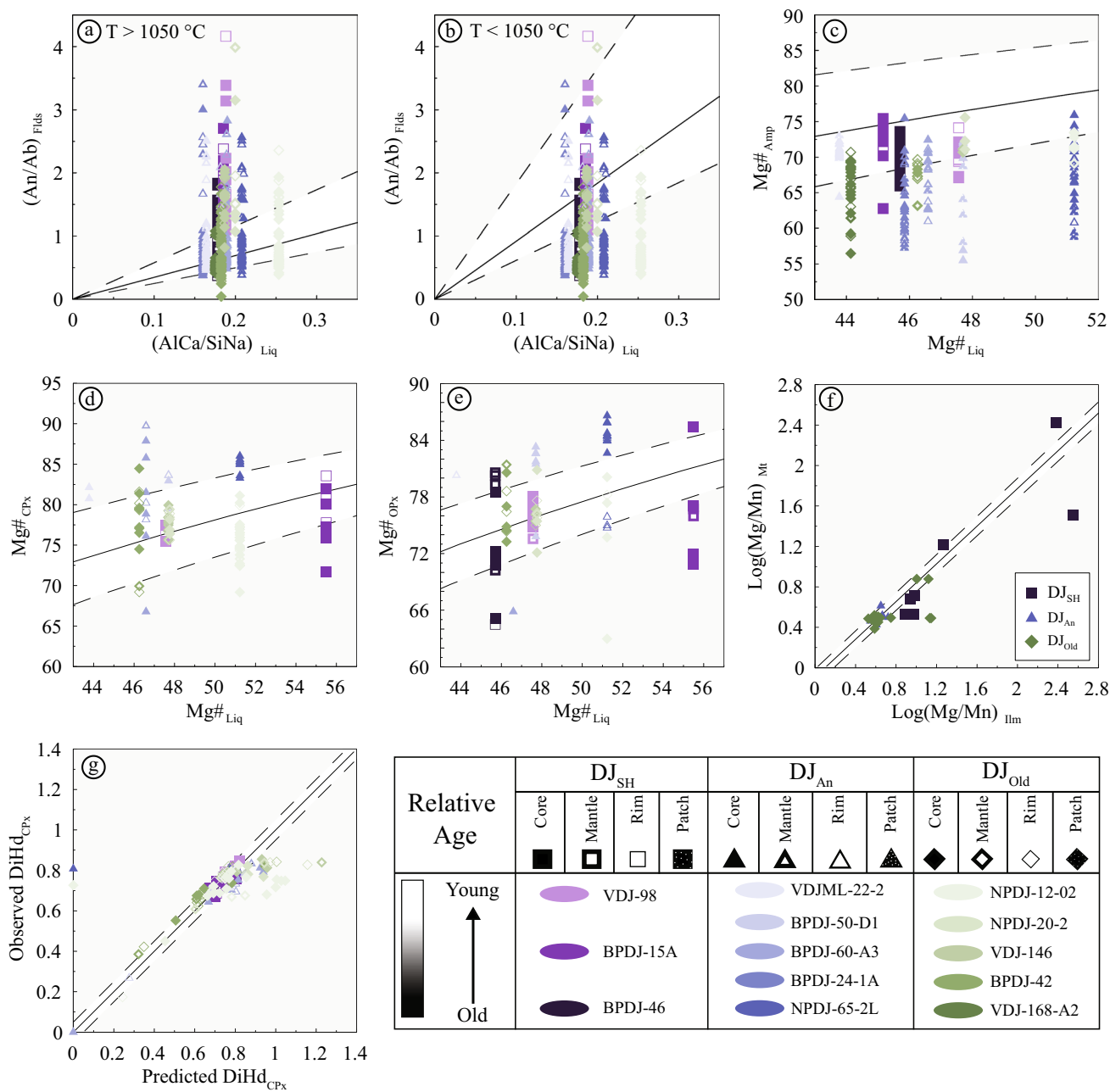
Fig. 7 Equilibrium test diagrams for (**a**) Plagioclase using Putirka(2008) high-T Kd, (**b**) Plagioclase using Putirka (2008) low-T Kd; (**c**) Amphibole using Putirka (2016) Kd, (**d**) clinopyroxene, and (**e**) orthopyroxene, using their corresponding Kds from Putirka (2008); (**f**) Diopside-hedenbergite component diagram; (**g**) Ilmenite-magnetite pairs following Bacon and Hirschmann (1988)

to matrix effects during EPMA analysis, leading us not to consider these data in our interpretations. As these temperatures frequently reflect subsolidus reequilibration, they were compared with the single-mineral (Mt) geothermometer of Canil and Lacourse (2020), which is based on the strong temperature dependence of the Mg molar fraction in Mt. Magnetite-ilmenite pairs ($n = 5$ for DJ_{SH}, 9 for DJ_{An}, and 17 for DJ_{Old}) yielded 873–838 °C at ranges of $\log fO_2$ between −11 and −12 for DJ_{SH}; 844–638 °C at $\log fO_2$ between −12

and −19 for DJ_{An}, and 828 to 747 °C, at $\log fO_2$ from −12 to −15 for DJ_{Old}. These temperatures are in good agreement with single-mineral (Mt) temperatures (SEE $\pm$ 50 °C) of 1063–859 °C for DJ_{SH}, and 908–781 °C for DJ_{An}, whereas for $DJ_{Old,}$ single-mineral temperatures display a wider range compared to Mt-Ilm temperatures, yielding 1044–745 °C (Supplementary Material SMA3.8).

Finally, Amp data passing the equilibrium tests were used as an exploratory approach to preliminarily estimate
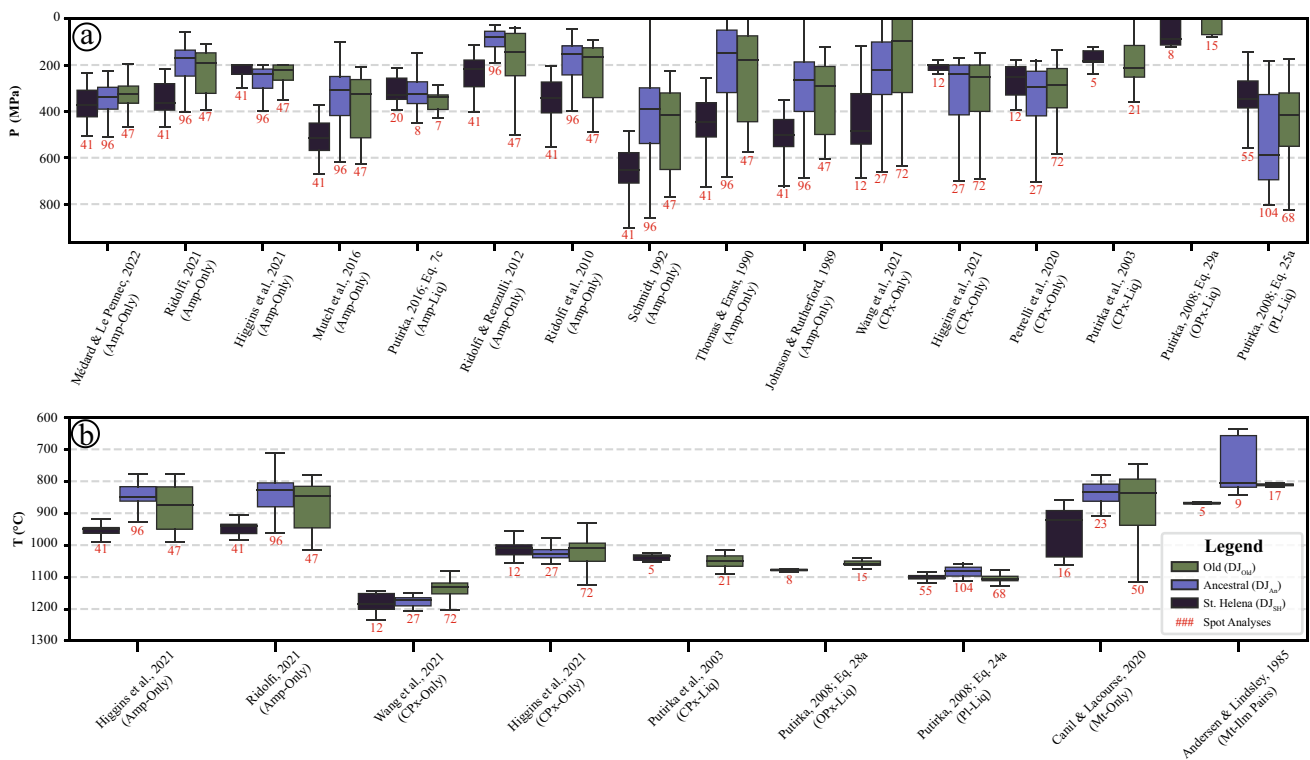
Fig. 8 Box diagrams with results from pressure (**a**, MPa) and temperature (**b**, °C) geothermobarometry estimations from samples of the Pleistocene DJVC edifices. Tick labels in the horizontal axes indicate each model's publication reference and its type (e.g., mineral-liquid pair, mineral–mineral pair, mineral-only). In order of vertical appearance, horizontal lines in each box represent the minimum, median, and maximum value within the set of estimations. Results from mineral-liquid, and mineral–mineral pair models only take into accounts pressure or temperature values from spot analyses that passed equilibrium tests. Results from mineral-only models include values from all available spot analyses

pre-eruptive H_2O_{melt} contents (SEE: $\pm 14\%$) between 7 and 4 wt% at $\log fO_2$ (SEE: ± 0.3 log units) of -8 to -11 for DJ_{SH}; between 6 and 5 wt% at $\log fO_2$ of -8 and -11 for DJ_{An}; and between 6 and 4 wt% at $\log fO_2$ of -6 and -10 for DJ_{Old} (Supplementary Material SMA3.2). However, these results must be handled with caution and should be validated through comparison with future work on melt inclusions.

Magma differentiation and pre-eruptive storage conditions

The decreasing linear trends of major and trace elements vs. silica content observed in whole-rock compositions indicate that fractional crystallization plays a significant role explaining the mineral assemblages identified. This process is evaluated as a potential mechanism for magmatic differentiation using major elements, aiming to establish (a) the composition of the potential parental magma for Doña Juana melts, (b) the conditions of magma evolution and fractionation (crystallization pressures and temperatures) and the extent of fractional crystallization required to reproduce DJVC dacitic

melts, and (c) the fractionated mineral assemblage governing the fractional crystallization process.

To analyze magmatic differentiation within the Pleistocene DJVC storage system, a major-element, closed-system, fractional crystallization model was implemented using the Rhyolite-MELTS v.1.2.0. algorithm (Gualda et al. 2012; Ghiorso and Gualda 2015). The coeval basaltic and basaltic andesitic bombs of the neighboring Granatífera Tuff (with a Mg# range of 56–73) serve as proxies for near-primary arc magmas (Zieman et al. 2023, 2024). Consequently, sample MXL09-B4 from Zieman et al. (2024)—with a MgO content of 9.04 wt%—is considered the most closely resembling, natural, major-element composition to a primary magma, and was selected as the starting point for the model. Different models were tested under isobaric conditions, encompassing initial and final pressures between 400 and 200 MPa, initial and final temperatures between 1245 °C and 700 °C (with cooling steps of 5 °C), variable water contents in accordance with the presence of hydrous mineral phases such as Bt and Amp (1, 1.5, and 2 wt%), and an oxygen fugacity fixed relative to the QFM (quartz-fayalite-magnetite) buffer.

Samples from Pleistocene DJVC are best reproduced by an isobaric fractional crystallization model starting at a pressure of ~ 300 MPa, initial H_2O content of 1.5 wt%, initial liquidus temperature of 1225 °C, final liquidus temperature of 800 °C, and initial and final $log fO_2$ of −7.8 and −14.18, respectively. The best-fit model results are displayed in Fig. 9 and registered in the Supplementary Material SMA4. The model's resulting liquid line of descent (i.e., residual melt compositions) closely matches the compositions of Pleistocene DJVC magmas. This includes the following fractionated mineral sequence (Fig. 9): Ol (1225–1200 °C), OPx (1195–765 °C), CPx (1150–800 °C), Pl (1135–800 °C), and Sp (1060–805 °C). The model also indicates the crystallization of a second CPx phase at 1075°C, with lower TiO_2, CaO, Al_2O_3, Na_2O, and higher SiO_2, MgO, and FeO_T than the first CPx, likely representing the hydrated mafic mineral phases (Amp and Bt) not included in the Rhyolite-MELTS v.1.2.0 database (Ghiorso and Gualda 2015). The calculated melts in equilibrium with the analyzed CPx and Amp mineral phases reconstructed from the models of Higgins et al. (2022) also fit the modeled liquid line of descent for DJVC samples, with compositions standing between those of the Granatífera Tuff and DJVC magmas.

In addition, the incompatible behavior of K_2O and most of the LILEs is consistent with the enrichment of these elements with magmatic differentiation as the volatile content increases. These processes stimulate the crystallization of hydrated phases, such as amphibole and biotite, both identified in the paragenesis of samples. The slightly compatible behavior of MREE and strongly compatible HREEs are also consistent with the presence of said hydrous mafic phases along with apatite and zircon, which are common accessory minerals.

In summary, we demonstrate that the basaltic bombs of the neighboring Granatífera Tuff likely represent the parental magma composition for DJVC. Such magma could evolve predominantly by extensive fractional crystallization, with degrees between 55% and 75%, toward the DJVC compositions within nearly isobaric conditions (~ 300 MPa). Assuming an average density of 2800 kg/m^3 for arc lithosphere in the Northern Andes consistent with the density structure reported for the region by Sanchez-Rojas and Palma (2014), and excluding unreasonable (e.g., negative) Pl-liquid and OPx-liquid barometry results, pressures obtained here by multiple barometers could only resolve broad storage depths in the middle crust, between ~ 18 to ~ 7 km for DJ_{SH}, ~ 12 to ~ 8 km for DJ_{An}, and ~ 15 to ~ 5 km for DJ_{Old}. Low Amp-only and CPx-only barometers resolved shallow crystallization conditions (probably microcrysts within the uppermost plumbing system) to 3 in DJ_{An}, and 5 km in DJ_{Old}.
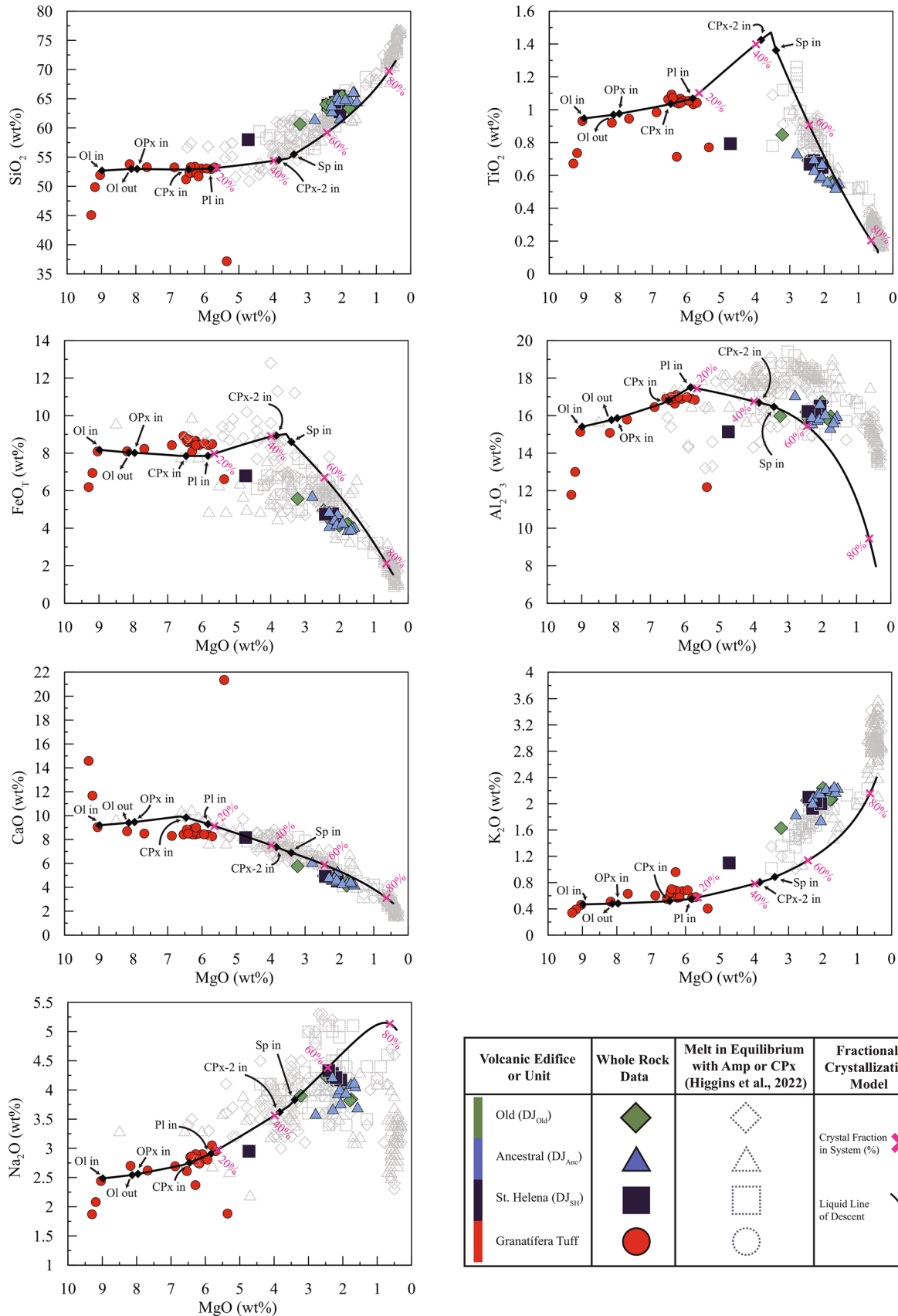
However, even if the available geothermobarometers for these compositions do not reach a good resolution for the middle crust, the coexistence of similar sized crystals showing variable (equilibrium and disequilibrium) textures and geochemical compositions points toward the assemblage of diverse crystal cargos in the uppermost storage region before their final eruption, consistent with the existence of a TCMS (Fig. 10). Pl textural types in DJVC best reflect the complexity of this TCMS, with felsic (An_{20-40} antecrysts) core populations showing deformation twins and serrated grain boundaries typical of intrusive feldspars. This is consistent with coexisting quartz macrocrysts and Fe-Ti oxides microaggregates showing exsolution lamellae. This presence of multiple crystal populations has been observed in several arc volcanoes and supports evidence of crystal entrainment from different textural domains (Ginibre et al. 2002; Cooper and Reid 2003; Wallace and Bergantz 2004; Berlo et al. 2007; Andrews et al. 2008; Claiborne et al. 2010; Ruprecht et al. 2012; Cashman and Blundy 2013; Sosa-Ceballos et al. 2014; Wanke et al. 2019). Different crystallization histories suggesting multiple textural domains explain, for instance, felsic crystal cores residing in cooler and evolved parts of the TCMS before entrainment and transport by a hotter melt into shallower levels (Cashman and Blundy 2013; Giordano and Caricchi 2022).

Hence, our methodological approach to best apply geothermobarometry resolves the region where the TCMS developed in the middle crust, and our major-element, closed-system fractional crystallization model explains—to a large extent—the observed sample paragenesis. Crystallization temperatures retrieved here reflect nearly similar saturation conditions for Pl (1102–1080 °C), CPx (1009–1185 °C), and OPx (1059–1077 °C) throughout the Pleistocene. Amp and Mt-Ilm pairs appeared at consistently lower temperatures and suggest slightly hotter saturation conditions in the eldest edifice storage system (Amp: 950–940 °C; Mt-Il: 873–838 °C) compared to the intermediate (Amp: 850–823 °C; Mt-Ilm: 844–638 °C) and youngest edifices (Amp: 875–845 °C; Mt-Ilm: 828–747 °C) here studied.

However, the textural evidence (i.e., coexisting crystals of a particular mineral phase and equal size, showing equilibrium and disequilibrium textures, and coexisting olivine and quartz in the same rock), together with the dispersion in binary plots of LREE, MREE, most HSFE, some LILEs, Co, and some major elements (Al_2O_3, P_2O_5, K_2O, and Na_2O), suggests that magmatic differentiation cannot be explained exclusively by fractional crystallization, but requires additional processes such as crustal contamination, magma recharge, and/or magma mixing (Tatsumi and Eggins 1995; Couch et al. 2001). In fact, a subtle effect of recharge processes in major element binary plots (Fig. 3) could also be inferred, as TiO_2, FeO_T, MgO, and CaO contents are always slightly higher in average for DJ_{SH} and DJ_{Old} than for DJ_{An}.

In addition, the significantly higher contents of hydrated mafic phases (biotite and amphibole) in DJ_{An}—along with

◄**Fig. 9** Major elements concentrations versus MgO (wt %) for the Pleistocene DJVC units. Solid black line represents the evolution path of residual melts modeled using the Rhyolite-MELTS v.1.2.0. algorithm (Gualda et al. 2012; Ghiorso and Gualda 2015); pink crosses mark steps of 20% fractional crystallization. The best-fit fractional crystallization model (solid black line) has an initial pressure of 300 MPa (isobaric), initial H_2O content of 1.5 wt%, initial liquidus temperature of 1225 °C, final liquidus temperature of 800 °C, and initial and final log$f$O$_2$ of -7.8 and -14.18, respectively. Sample MXL09-B4 from Zieman et al. (2024) of the neighboring Granatífera Tuff was considered as the starting point (closest composition to a primary magma). The calculated theoretical melts in equilibrium with CPx and Amp (Higgins et al. 2022) are also plotted for comparison

the presence of Mg-hornblende—indicates that the silica content and volatile budget within the TCMS increased after the first volcano-tectonic collapse (vt; Pardo et al. 2019). Slightly lower Amp temperatures in DJ$_{An}$ compared to the eldest and youngest edifices reflect the effect of silica content in the maximum temperature for amphibole stability (Sato et al. 1999). Moreover, the sharp change in magnetite geochemistry recorded by DJ$_{An}$ samples with lower TiO$_2$, Al$_2$O$_3$, and MgO contents, and strongly MnO-enriched and MgO-depleted ilmenite exsolutions compared to their DJ$_{SH}$ counterparts, suggests lower crystallization temperatures consistent with a system evolving mainly by fractional crystallization $\pm$ assimilation. This contrasts with evidence from DJ$_{SH}$ and DJ$_{Old}$, where recharge and mixing events seem more prominent. In similar arc systems elsewhere, mush disaggregation and its transition toward eruptible magma is commonly induced by injection of deeper, hotter, and/or volatile richer melts in the weeks to years before the eruption (Claiborne et al. 2010; Allan et al. 2013; Moore et al. 2014). In the case of DJVC, the rejuvenation of the mush is inferred from decreasing felsic An$_{20-40}$ data in Pl cores and increasing Mg# in Amp cores over time within each edifice, particularly in DJ$_{SH}$ and DJ$_{Old}$. The higher presence of felsic antecryst cores at the beginning of each stratigraphic succession also suggests that the cyclic edifice growth after each major collapse seems to be accompanied by a mush disaggregation event.

Our results suggest that the Pleistocene storage system below the DJVC was subject to the frequent production and injection of mafic magmas in a region where arc roots exhibit high temperatures (as registered by the lower-crustal xenoliths entrained in the Granatífera Tuff: 720–850 °C at ~ 30–40 km, proper of the lower crust; and 920–1280 °C at roughly 30–70 km, which corresponds to the lower lithosphere; Weber et al. 2002; Bloch et al. 2017; Zieman et al. 2023). Although further diffusion chronology studies are required, final recharge by mafic injection as potential eruption triggering mechanism (Andrews et al. 2008) is attested by several examples of crystals with An-and-Mg#-rich rims compared to the corresponding cores in all samples. Increasing modal proportions of hydrated (i.e., Bt, Amp) and silica

saturation-dependent phases (e.g., Mg-hornblende), along with sharp changes in magnetite composition and slight variations in Amp-recorded temperatures, can be explained as a consequence of the injection of hotter, more volatile-rich melts into crystallizing reservoirs. These injections are particularly prevalent in the intermediate volcanic edifice (DJ$_{An}$) built after the first known volcano-tectonic collapse (vt). In fact, the frequency of these injections makes them potential eruption-triggering events to be studied in future work, as attested by the increasingly higher proportional contents of Ca and Mg, respectively, observed in plagioclase and amphibole cores within samples of all edifices.

In general, our results are consistent with disequilibrium textures and petrogenetic models retrieved for neighboring dacitic volcanoes in northern Ecuador, where mid-crustal (~ 5–20 km) crystal mushes subject to rejuvenation and mafic injections are known to feed volcanism (Ridolfi et al. 2008; Stewart and Castro 2016; Saalfeld et al. 2019; Koch et al. 2021).

Conclusions

The Pleistocene history of the remote Doña Juana Volcanic Complex adds a new example of the presence of trans-crustal magmatic systems in the poorly documented Colombian Andes. For the first time in the study of Colombian composite volcanoes, we reconstructed the physicochemical conditions of the most likely melt–mush interaction zone involved in Pleistocene volcanism. By applying multiple geothermobarometers and testing equilibrium conditions, specific, individual storage levels within a TCMS cannot be resolved, but we were able to establish that the extent of melt–mush interaction zone encompasses depths between ~ 18 and 5 km under the surface. Under nearly isobaric conditions, geochemical trends of major elements suggest that fractional crystallization of Pl + CPx + OPx + Amp + Bt + Mt-Ilm from a basaltic primary magma sampled by a neighboring source of mafic and xenolith-rich ignimbrite volcanism plays a predominant role in shaping the composition of the monotonously dacitic eruptive products. The Pleistocene history of the Doña Juana Volcanic Complex is—consequently—that of a dacitic volcanic center fed by a trans-crustal magmatic system where melts accumulate as a crystal mush who evolved predominantly through fractional crystallization (and crustal assimilation), but was constantly subject to the injection of and mixing with more primitive melts whose thermodynamic and compositional effects caused disequilibrium events leading to mush disaggregation, melt migration, and eventually eruption.

Given that geothermobarometry estimations using multiple single-mineral and mineral-melt models cannot resolve
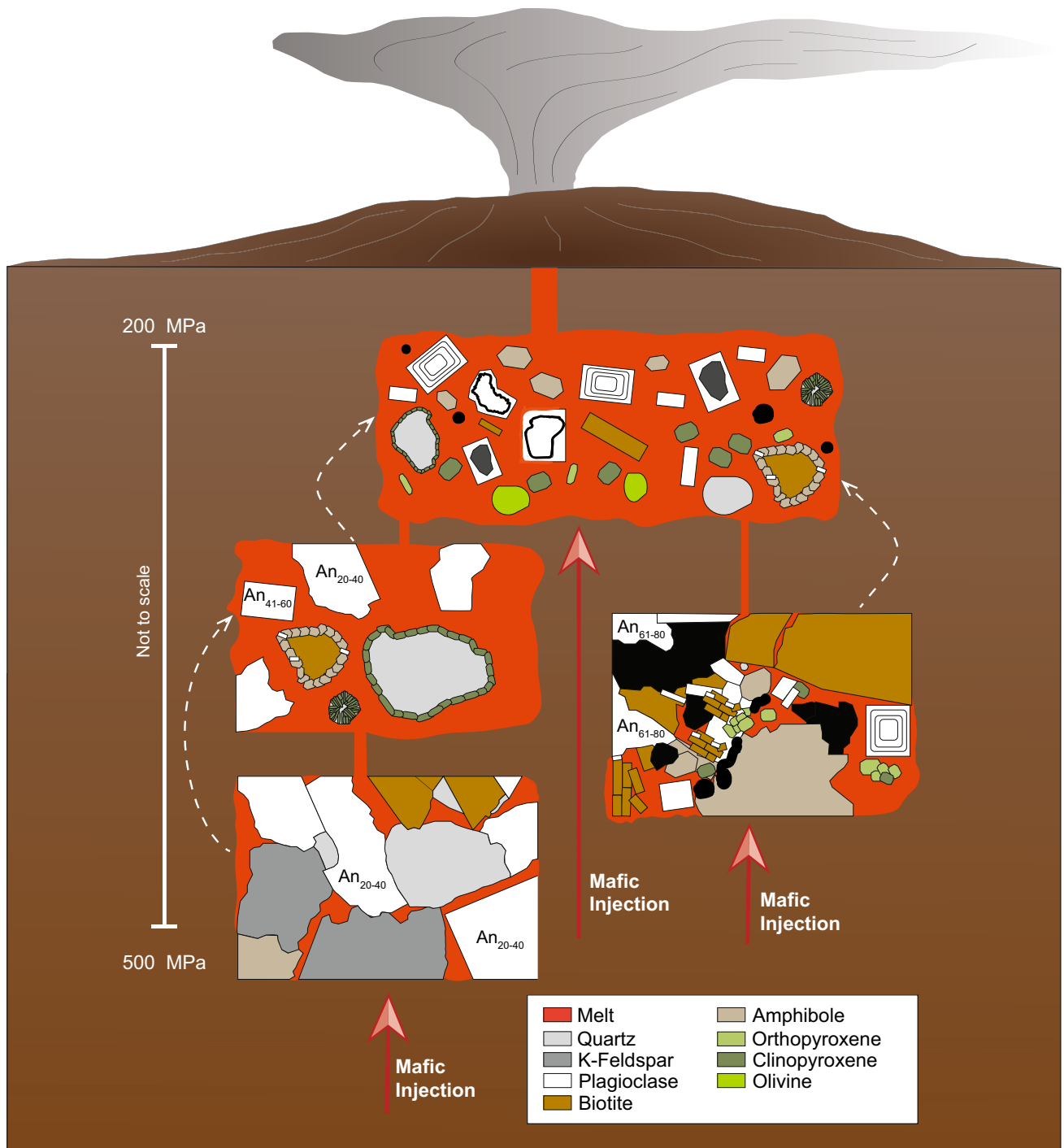
Fig. 10 Schematic model (not to scale) illustrating the complex TCMS expected below the DJVC, with multiple textural domains. Mush rejuvenation events by mafic injections allowed the establishment of a shallow storage level, at nearly 300 MPa, where antecrysts merged and isobaric crystallization explains most of the mineral paragenesis found in the DJVC monotonous dacites. Mafic injections within this uppermost level might also be responsible for final recharge and eruption

intensive parameters (i.e., P, T, fO_2, H_2O_{melt}) in the middle crust, melt and fluid inclusion analysis should be a major task required to realistically address and investigate the pre-eruptive conditions of the Doña Juana Volcanic Complex in the future. Detailed petrographic observations in these Andean complex dacitic systems are compulsory to identify numerous textures indicative of crystallization in both equilibrium and disequilibrium with their corresponding melt

before arbitrarily applying published thermobarometers. In these cases, mineral-liquid calibrations applied to phases tested for equilibrium fall within the error of mineral-only thermobarometers and seem to be valid where whole-rock geochemical variations are restricted over geological time, only after the consideration of textural and compositional constraints.

Author Contributions All co-authors contributed to the research project and the preparation of this document as follows: conceptualization was carried out by all authors. Field work and sample collection was done by N. Pardo and B.A. Pulgarín. Petrographic observations were carried out by N. Pardo, C. de Ignacio San José, M. Arnosio, and A.M. Correa. EPMA analysis was done by C. de Ignacio San José. Data compilation, processing, and artwork design were prepared by C- Bucheli-Olaya, P. Larrea, and N. Pardo. The manuscript was prepared by C. Bucheli-Olaya, N. Pardo, P. Larrea, and C. de Ignacio San José. All co-authors contributed, commented, or edited previous versions of this document. All authors read and approved the submission of this final manuscript.

Data availability Authors confirm that all data supporting these findings can be accessed to in the supplementary materials.

Declarations

Conflict of interest Most of the whole-rock samples and data were collected between 2005 and 2008 by the Colombian Geological Survey. Their corresponding geochemical analyses were presented on an internal report (Pardo et al. 2016), and major elements were published by Pardo et al. (2019). The use of these data and their interpretation in this manuscript lies within the working agreement "Convenio 035 de 2018 celebrado entre el Servicio Geológico Colombiano (SGC) y la Universidad de Los Andes." This research was partially funded by the FAPA grant allocated to Natalia Pardo, and by the "Fondo de Investigaciones de la Facultad de Ciencias de la Universidad de Los Andes INV-2023-162-2839," also allocated to N. Pardo.

References

Allan ASR, Morgan DJ, Wilson CJN, Millet M-A (2013) From mush to eruption in centuries: assembly of the super-sized Oruanui magma body. Contrib Mineral Petrol 166:143–164. https://doi.org/10.1007/s00410-013-0869-2

Andersen DJ, Lindsley DH (1985) New (and final!) models for the Ti-magnetite/ilmenite geothermometer and oxygen barometer. In: Abstracts of American Geophysical Union 1985 Spring Meeting. American Geophysical Union

Anderson AT (1976) Magma mixing: petrological process and volcanological tool. J Volcanol Geotherm Res 1:3–33. https://doi.org/10.1016/0377-0273(76)90016-0

Andrews BJ, Gardner JE, Housh TB (2008) Repeated recharge, assimilation, and hybridization in magmas erupted from El Chichón as recorded by plagioclase and amphibole phenocrysts. J Volcanol Geotherm Res 175:415–426. https://doi.org/10.1016/j.jvolgeores.2008.02.017

Annen C, Sparks RSJ (2002) Effects of repetitive emplacement of basaltic intrusions on thermal evolution and melt generation in the crust. Earth Planet Sci Lett 203:937–955. https://doi.org/10.1016/S0012-821X(02)00929-9

Annen C, Blundy JD, Sparks RSJ (2006) The genesis of intermediate and silicic magmas in deep crustal hot zones. J Petrol 47:505–539. https://doi.org/10.1093/petrology/egi084

Bachmann O, Huber C (2016) Silicic magma reservoirs in the Earth's crust. Am Mineral 101:2377–2404. https://doi.org/10.2138/am-2016-5675

Bacon CR, Hirschmann MM (1988) Mg/Mn partitioning as a test for equilibrium between coexisting Fe-Ti oxides. Am Mineral 73:57–61

Barberi F, Coltelli M, Ferrara G et al (1988) Plio-Quaternary volcanism in Ecuador. Geol Mag 125:1–14. https://doi.org/10.1017/S0016756800009328

Berlo K, Blundy J, Turner S, Hawkesworth C (2007) Textural and chemical variation in plagioclase phenocrysts from the 1980 eruptions of Mount St. Helens, USA. Contrib Mineral Petrol 154:291–308. https://doi.org/10.1007/s00410-007-0194-8

Bloch E, Ibañez-Mejia M, Murray K et al (2017) Recent crustal foundering in the Northern Volcanic Zone of the Andean arc: petrological insights from the roots of a modern subduction zone. Earth Planet Sci Lett 476:47–58. https://doi.org/10.1016/j.epsl.2017.07.041

Canil D, Lacourse T (2020) Geothermometry using minor and trace elements in igneous and hydrothermal magnetite. Chem Geol 541:119576. https://doi.org/10.1016/j.chemgeo.2020.119576

Cashman K, Blundy J (2013) Petrological cannibalism: the chemical and textural consequences of incremental magma body growth. Contrib Mineral Petrol 166:703–729. https://doi.org/10.1007/s00410-013-0895-0

Cashman KV, Sparks RSJ, Blundy JD (2017) Vertically extensive and unstable magmatic systems: a unified view of igneous processes. Science 355:eaag3055. https://doi.org/10.1126/science.aag3055

Claiborne LL, Miller CF, Flanagan DM et al (2010) Zircon reveals protracted magma storage and recycling beneath Mount St. Helens Geology 38:1011–1014. https://doi.org/10.1130/G31285.1

Comeau MJ, Unsworth MJ, Ticona F, Sunagua M (2015) Magnetotelluric images of magma distribution beneath Volcán Uturuncu, Bolivia: implications for magma dynamics. Geology 43:243–246. https://doi.org/10.1130/G36258.1

Cooper KM, Reid MR (2003) Re-examination of crystal ages in recent Mount St. Helens lavas: implications for magma reservoir processes. Earth Planet Sci Lett 213:149–167. https://doi.org/10.1016/S0012-821X(03)00262-0

Couch S, Sparks RSJ, Carroll MR (2001) Mineral disequilibrium in lavas explained by convective self-mixing in open magma chambers. Nature 411:1037–1039. https://doi.org/10.1038/35082540

DePaolo DJ (1981) Trace element and isotopic effects of combined wallrock assimilation and fractional crystallization. Earth Planet Sci Lett 53:189–202. https://doi.org/10.1016/0012-821X(81)90153-9

Droux A, Delaloye M (1996) Petrography and geochemistry of Plio-Quaternary calc-alkaline volcanoes of Southwestern Colombia. J South Am Earth Sci 9:27–41. https://doi.org/10.1016/0895-9811(96)00025-9

Gardner JE, Carey S, Rutherford MJ, Sigurdsson H (1995a) Petrologic diversity in Mount St. Helens dacites during the last 4,000 years: implications for magma mixing. Contrib Mineral Petrol 119:224–238. https://doi.org/10.1007/BF00307283

Gardner JE, Rutherford M, Carey S, Sigurdsson H (1995b) Experimental constraints on pre-eruptive water contents and changing magma storage prior to explosive eruptions of Mount St Helens volcano. Bull Volcanol 57:1–17. https://doi.org/10.1007/BF00298703

Geiger H, Barker AK, Troll VR (2016) Locating the depth of magma supply for volcanic eruptions, insights from Mt. Cameroon Sci Rep 6:33629. https://doi.org/10.1038/srep33629

Ghiorso MS, Evans BW (2008) Thermodynamics of rhombohedral oxide solid solutions and a revision of the FE-TI two-oxide geothermometer and oxygen-barometer. Am J Sci 308:957–1039. https://doi.org/10.2475/09.2008.01

Ghiorso MS, Gualda GAR (2015) An H_2O–CO_2 mixed fluid saturation model compatible with rhyolite-MELTS. Contrib Mineral Petrol 169:53. https://doi.org/10.1007/s00410-015-1141-8

Giacomoni PP, Casetta F, Valenti V et al (2021) Thermo-barometric constraints on the Mt. Etna 2015 eruptive event. Contrib Mineral Petrol 176:88. https://doi.org/10.1007/s00410-021-01848-8

Ginibre C, Wörner G, Kronz A (2002) Minor- and trace-element zoning in plagioclase: implications for magma chamber processes at Parinacota volcano, northern Chile. Contrib Mineral Petrol 143:300–315. https://doi.org/10.1007/s00410-002-0351-z

Giordano G, Caricchi L (2022) Determining the state of activity of transcrustal magmatic systems and their volcanoes. Annu Rev Earth Planet Sci 50:231–259. https://doi.org/10.1146/annurev-earth-032320-084733

Gualda GAR, Ghiorso MS, Lemons RV, Carley TL (2012) Rhyolite-MELTS: a modified calibration of MELTS optimized for silica-rich, fluid-bearing magmatic systems. J Petrol 53:875–890. https://doi.org/10.1093/petrology/egr080

Gutscher M-A, Malavieille J, Lallemand S, Collot J-Y (1999) Tectonic segmentation of the North Andean margin: impact of the Carnegie Ridge collision. Earth Planet Sci Lett 168:255–270. https://doi.org/10.1016/S0012-821X(99)00060-6

Hall ML, Wood CA (1985) Volcano-tectonic segmentation of the northern Andes. Geology 13:203–207. https://doi.org/10.1130/0091-7613(1985)13%3c203:VSOTNA%3e2.0.CO;2

Higgins O, Sheldrake T, Caricchi L (2022) Machine learning thermobarometry and chemometry using amphibole and clinopyroxene: a window into the roots of an arc volcano (Mount Liamuiga, Saint Kitts). Contrib Mineral Petrol 177:10. https://doi.org/10.1007/s00410-021-01874-6

Hildreth W, Moorbath S (1988) Crustal contributions to arc magmatism in the Andes of Central Chile. Contrib Mineral Petrol 98:455–489. https://doi.org/10.1007/BF00372365

Humphreys MCS, Blundy JD, Sparks RSJ (2006) Magma evolution and open-system processes at Shiveluch Volcano: insights from phenocryst zoning. J Petrol 47:2303–2334. https://doi.org/10.1093/petrology/egl045

Idárraga-García J, Kendall J-M, Vargas CA (2016) Shear wave anisotropy in northwestern South America and its link to the Caribbean and Nazca subduction geodynamics: Seismic Anisotropy in New South America. Geochem Geophys Geosystems 17:3655–3673. https://doi.org/10.1002/2016GC006323

James DE, Murcia LA (1984) Crustal contamination in northern Andean volcanics. J Geol Soc 141:823–830. https://doi.org/10.1144/gsjgs.141.5.0823

Jarosewich E, Nelen JA, Norberg JA (1980) Reference samples for electron microprobe analysis*. Geostand Geoanalytical Res 4:43–47. https://doi.org/10.1111/j.1751-908X.1980.tb00273.x

Johnson MC, Rutherford MJ (1989) Experimental calibration of the aluminum-in-hornblende geobarometer with application to Long Valley caldera (California) volcanic rocks. Geology 17:837. https://doi.org/10.1130/0091-7613(1989)017%3c0837:ECOTAI%3e2.3.CO;2

Koch CD, Delph J, Beck SL et al (2021) Crustal thickness and magma storage beneath the Ecuadorian arc. J South Am Earth Sci 110:103331. https://doi.org/10.1016/j.jsames.2021.103331

Le Bas MJ, Le Maitre RW, Streckeisen A et al (1986) A chemical classification of volcanic rocks based on the total alkali-silica diagram. J Petrol 27:745–750. https://doi.org/10.1093/petrology/27.3.745

Le Maitre P, Streckeisen A, Zanettin B et al (eds) (2002) Igneous rocks: a classification and glossary of terms: recommendations of the International Union of Geological Sciences Subcommission on the systematics of igneous rocks, 2nd edn. Cambridge University Press, Cambridge

Macías JL, Sosa-Ceballos G, Arce JL et al (2017) Storage conditions and magma processes triggering the 1818 CE Plinian eruption of Volcán de Colima. J Volcanol Geotherm Res 340:117–129. https://doi.org/10.1016/j.jvolgeores.2017.02.025

Marcaillou B, Spence G, Wang K et al (2008) Thermal segmentation along the N. Ecuador–S. Colombia margin (1–4°N): prominent influence of sedimentation rate in the trench. Earth Planet Sci Lett 272:296–308. https://doi.org/10.1016/j.epsl.2008.04.049

McDonough WF, Sun S-S (1995) The composition of the Earth. Chem Geol 120:223–253

Médard E, Le Pennec J-L (2022) Petrologic imaging of the magma reservoirs that feed large silicic eruptions. Lithos 428–429:106812. https://doi.org/10.1016/j.lithos.2022.106812

Mojica Boada MJ, Poveda E, Tary JB (2022) Lithospheric and slab configurations from receiver function imaging in Northwestern South America, Colombia. J Geophys Res Solid Earth 127:e2022JB024475. https://doi.org/10.1029/2022JB024475

Monsalve-Bustamante ML (2020) The volcanic front in Colombia: segmentation, recent and historical activity. In: The geology of Colombia. Servicio Geológico Colombiano, Bogotá

Moore A, Coogan LA, Costa F, Perfit MR (2014) Primitive melt replenishment and crystal-mush disaggregation in the weeks preceding the 2005–2006 eruption 9° 50′ N, EPR. Earth Planet Sci Lett 403:15–26. https://doi.org/10.1016/j.epsl.2014.06.015

Mutch EJF, Blundy JD, Tattitch BC et al (2016) An experimental study of amphibole stability in low-pressure granitic magmas and a revised Al-in-hornblende geobarometer. Contrib Mineral Petrol 171:85. https://doi.org/10.1007/s00410-016-1298-9

Pardo N, Pulgarín B, Betancourt V et al (2019) Facing geological mapping at low-latitude volcanoes: the Doña Juana Volcanic Complex study-case, SW-Colombia. J Volcanol Geotherm Res 385:46–67. https://doi.org/10.1016/j.jvolgeores.2018.04.016

Pardo N, Pulgarín-Alzate B, Betancourt Suárez V (2016) Avances en el conocimiento geológico sobre el complejo Volcánico Doña Juana: integración del análisis de litofacies, estratigrafía, geocronología y petrología. Internal report for the Colombian Geological Survey. 530 p. https://miig.sgc.gov.co/Paginas/Resultados.aspx?k=Pardo%2C%20estratigraf%C3%ADa%2C%20Do%C3%B1a%20Juana

Pardo N, Sulpizio R, Lucchi F et al (2023) Late Holocene volcanic stratigraphy and eruption chronology of the dacitic Young Doña Juana volcano, Colombia. GSA Bull. https://doi.org/10.1130/B36557.1

Pelullo C, Iovine RS, Arienzo I et al (2022) Mineral-melt equilibria and geothermobarometry of Campi Flegrei Magmas: inferences for magma storage conditions. Minerals 12:308. https://doi.org/10.3390/min12030308

Pennington WD (1981) Subduction of the Eastern Panama Basin and seismotectonics of northwestern South America. J Geophys Res Solid Earth 86:10753–10770. https://doi.org/10.1029/JB086iB11p10753

Petrelli M, Caricchi L, Perugini D (2020) Machine learning thermobarometry: application to clinopyroxene-bearing magmas. J Geophys Res Solid Earth 125:e2020JB020130. https://doi.org/10.1029/2020JB020130

Petrone CM, Mollo S, Gertisser R et al (2022) Magma recharge and mush rejuvenation drive paroxysmal activity at Stromboli volcano. Nat Commun 13:7717. https://doi.org/10.1038/s41467-022-35405-z

Powell R, Powell M (1977) Geothermometry and oxygen barometry using coexisting iron-titanium oxides: a reappraisal. Mineral Mag 41:257–263. https://doi.org/10.1180/minmag.1977.041.318.14

Putirka KD (2008) Thermometers and barometers for volcanic systems. Rev Mineral Geochem 69:61–120. https://doi.org/10.2138/rmg.2008.69.3

Putirka K (2016) Special collection: rates and depths of magma ascent on Earth: amphibole thermometers and barometers for igneous systems and some implications for eruption mechanisms of felsic magmas at arc volcanoes. Am Mineral 101:841–858. https://doi.org/10.2138/am-2016-5506

Putirka KD, Mikaelian H, Ryerson F, Shaw H (2003) New clinopyroxene-liquid thermobarometers for mafic, evolved, and volatile-bearing lava compositions, with applications to lavas from Tibet and the Snake River Plain, Idaho. Am Mineral 88:1542–1554. https://doi.org/10.2138/am-2003-1017

Rhodes JM, Dungan MA, Blanchard DP, Long PE (1979) Magma mixing at mid-ocean ridges: evidence from basalts drilled near 22° N on the Mid-Atlantic Ridge. Tectonophysics 55:35–61. https://doi.org/10.1016/0040-1951(79)90334-2

Ridolfi F (2021) Amp-TB2: an updated model for calcic amphibole thermobarometry. Minerals 11:324. https://doi.org/10.3390/min11030324

Ridolfi F, Renzulli A (2012) Calcic amphiboles in calc-alkaline and alkaline magmas: thermobarometric and chemometric empirical equations valid up to 1,130°C and 2.2 GPa. Contrib Mineral Petrol 163:877–895. https://doi.org/10.1007/s00410-011-0704-6

Ridolfi F, Puerini M, Renzulli A et al (2008) The magmatic feeding system of El Reventador volcano (Sub-Andean zone, Ecuador) constrained by texture, mineralogy and thermobarometry of the 2002 erupted products. J Volcanol Geotherm Res 176:94–106. https://doi.org/10.1016/j.jvolgeores.2008.03.003

Ridolfi F, Renzulli A, Puerini M (2010) Stability and chemical equilibrium of amphibole in calc-alkaline magmas: an overview, new thermobarometric formulations and application to subduction-related volcanoes. Contrib Mineral Petrol 160:45–66. https://doi.org/10.1007/s00410-009-0465-7

Ridolfi F, Zanetti A, Renzulli A et al (2018) AMFORM, a new mass-based model for the calculation of the unit formula of amphiboles from electron microprobe analyses. Am Mineral 103:1112–1125. https://doi.org/10.2138/am-2018-6385

Ruprecht P, Bergantz GW, Cooper KM, Hildreth W (2012) The crustal magma storage system of Volcán Quizapu, Chile, and the effects of magma mixing on magma diversity. J Petrol 53:801–840. https://doi.org/10.1093/petrology/egs002

Saalfeld MA, Kelley DF, Panter KS (2019) Insight on magma evolution and storage through the recent eruptive history of Cotopaxi Volcano, Ecuador. J South Am Earth Sci 93:85–101. https://doi.org/10.1016/j.jsames.2019.04.019

Sanchez-Rojas J, Palma M (2014) Crustal density structure in northwestern South America derived from analysis and 3-D modeling of gravity and seismicity data. Tectonophysics 634:97–115. https://doi.org/10.1016/j.tecto.2014.07.026

Sato H, Nakada S, Fujii T et al (1999) Groundmass pargasite in the 1991–1995 dacite of Unzen volcano: phase stability experiments and volcanological implications. J Volcanol Geotherm Res 89:197–212. https://doi.org/10.1016/S0377-0273(98)00132-2

Schmidt MW (1992) Amphibole composition in tonalite as a function of pressure: an experimental calibration of the Al-in-hornblende barometer. Contrib Mineral Petrol 110:304–310. https://doi.org/10.1007/BF00310745

Schneider CA, Rasband WS, Eliceiri KW (2012) NIH image to ImageJ: 25 years of image analysis. Nat Methods 9:671–675. https://doi.org/10.1038/nmeth.2089

Smith IEM, Németh K (2017) Source to surface model of monogenetic volcanism: a critical review. Geol Soc Lond Spec Publ 446:1–28. https://doi.org/10.1144/SP446.14

Smith VC, Blundy JD, Arce JL (2009) A temporal record of magma accumulation and evolution beneath Nevado de Toluca, Mexico, preserved in plagioclase phenocrysts. J Petrol 50:405–426. https://doi.org/10.1093/petrology/egp005

Solano JMS, Jackson MD, Sparks RSJ et al (2012) Melt segregation in deep crustal hot zones: a mechanism for chemical differentiation, crustal assimilation and the formation of evolved magmas. J Petrol 53:1999–2026. https://doi.org/10.1093/petrology/egs041

Sosa-Ceballos G, Gardner JE, Lassiter JC (2014) Intermittent mixing processes occurring before Plinian eruptions of Popocatepetl volcano, Mexico: insights from textural–compositional variations in plagioclase and Sr–Nd–Pb isotopes. Contrib Mineral Petrol 167:966. https://doi.org/10.1007/s00410-014-0966-x

Sparks SRJ, Sigurdsson H, Wilson L (1977) Magma mixing: a mechanism for triggering acid explosive eruptions. Nature 267:315–318. https://doi.org/10.1038/267315a0

Sparks RSJ, Annen C, Blundy JD et al (2019) Formation and dynamics of magma reservoirs. Philos Trans R Soc Math Phys Eng Sci 377:20180019. https://doi.org/10.1098/rsta.2018.0019

Spencer KJ, Lindsley DH (1981) A solution model for coexisting iron–titanium oxides. Am Mineral 66:1189–1201

Stern CR (2004) Active Andean volcanism: its geologic and tectonic setting. Rev Geológica Chile 31:161–206

Stewart A-M, Castro JM (2016) P-T–X evolution of the 1280 AD Quilotoa dacite. J Volcanol Geotherm Res 313:29–43. https://doi.org/10.1016/j.jvolgeores.2015.11.024

Sun M, Bezada MJ, Cornthwaite J et al (2022) Overlapping slabs: untangling subduction in NW South America through finite-frequency teleseismic tomography. Earth Planet Sci Lett 577:117253. https://doi.org/10.1016/j.epsl.2021.117253

Sun S-s, McDonough WF (1989) Chemical and isotopic systematics of oceanic basalts: implications for mantle composition and processes. Geol Soc Lond Spec Publ 42:313–345. https://doi.org/10.1144/GSL.SP.1989.042.01.19

Tatsumi, Eggins YS (1995) Subduction zone magmatism. Blackwell, Cambridge, MA

Thomas WM, Ernst WG (1990) The aluminum content of hornblende in calc-alkaline granitic rocks: a mineralogic barometer calibrated experimentally to 12 kbars. In: Spencer RJ, Chou I-M (eds) Fluid-mineral interactions: a tribute to H.P. Eugster, Special Publication No. 2. Geochemical Society, pp. 59–63

Thorpe RS, Francis PW (1979) Variations in andean andesite compositions and their petrogenetic significance. Tectonophysics 57:53–70. https://doi.org/10.1016/0040-1951(79)90101-X

Trenkamp R, Kellogg JN, Freymueller JT, Mora HP (2002) Wide plate margin deformation, southern Central America and northwestern South America, CASA GPS observations. J South Am Earth Sci 15:157–171. https://doi.org/10.1016/S0895-9811(02)00018-4

Vargas CA, Mann P (2013) Tearing and breaking off of subducted slabs as the result of collision of the Panama Arc-Indenter with Northwestern South America. Bull Seismol Soc Am 103:2025–2046. https://doi.org/10.1785/0120120328

Wallace GS, Bergantz GW (2004) Constraints on mingling of crystal populations from off-center zoning profiles: a statistical approach. Am Mineral 89:64–73. https://doi.org/10.2138/am-2004-0109

Wang X, Hou T, Wang M et al (2021) A new clinopyroxene thermobarometer for mafic to intermediate magmatic systems. Eur J Mineral 33:621–637. https://doi.org/10.5194/ejm-33-621-2021

Wanke M, Karakas O, Bachmann O (2019) The genesis of arc dacites: the case of Mount St. Helens, WA. Contrib Mineral Petrol 174:7. https://doi.org/10.1007/s00410-018-1542-6

Ward KM, Zandt G, Beck SL et al (2014) Seismic imaging of the magmatic underpinnings beneath the Altiplano-Puna volcanic complex from the joint inversion of surface wave dispersion and receiver functions. Earth Planet Sci Lett 404:43–53. https://doi.org/10.1016/j.epsl.2014.07.022

Weber MBI, Tarney J, Kempton PD, Kent RW (2002) Crustal make-up of the northern Andes: evidence based on deep crustal xenolith suites, Mercaderes, SW Colombia. Tectonophysics 345:49–82. https://doi.org/10.1016/S0040-1951(01)00206-2

Yarce J, Monsalve G, Becker TW et al (2014) Seismological observations in Northwestern South America: evidence for two subduction segments, contrasting crustal thicknesses and upper mantle flow. Tectonophysics 637:57–67. https://doi.org/10.1016/j.tecto.2014.09.006

Zieman L, Ibañez-Mejia M, Rooney AD et al (2023) To sink, or not to sink: the thermal and density structure of the modern northern Andean arc constrained by xenolith petrology. Geology 51:586–590. https://doi.org/10.1130/G50973.1

Zieman LJ, Ibañez-Mejia M, Tissot FLH et al (2024) Zirconium stable isotope fractionation during intra-crustal magmatic differentiation in an active continental arc. Geochim Cosmochim Acta 365:53–69. https://doi.org/10.1016/j.gca.2023.11.023